

## Green one-pot synthesis of pyrano[2,3-*c*]pyrazole monoazo dyes for high-performance textile dyeing and AgNP-enabled antimicrobial/UV functionalization

Ahmed Ragheb<sup>a</sup>, Maher H.Helal<sup>a</sup>, Saadia A. Abd El-Megied<sup>b</sup>, Fatma A. Mohamed<sup>b\*</sup> and Mohamed G. Abouelenein<sup>c\*</sup>

<sup>a</sup>Chemistry Department, Faculty of Science, Helwan University, Cairo, Egypt

<sup>b</sup>Dyeing, Printing and Auxiliaries Department, Institute for Textile Research and technology, National Research Center 33 El Buhouth St., Dokki, Giza, Postal code: 12622, Egypt

<sup>c</sup>Chemistry Department, Faculty of Science, Menoufia University, Shebin El-Koam, Menoufia, Postal code: 32519, Egypt

### CHRONICLE

#### Article history:

Received January 2, 2026

Received in revised form

January 10, 2026

Accepted March 5, 2026

Available online

March 5, 2026

#### Keywords:

Pyrano[2,3-*c*]pyrazole,

Synthesis

Monoazo dyes

Silver nanoparticles

Textile

Antibacterial textiles

### ABSTRACT

Despite extensive reports on azo dyes, the development of environmentally benign and multifunctional dye systems tailored for technical textiles remains limited. In this work, a green one-pot multicomponent strategy was employed to synthesize a series of pyrano[2,3-*c*]pyrazole-based monoazo dyes, which were structurally validated by comprehensive spectroscopic and elemental analyses. The dyes exhibited high exhaustion and fixation on polyester, nylon, and wool fabrics, delivering uniform deep shades with strong color strength, excellent fastness properties, and compatibility with high-temperature dyeing without auxiliary fixation steps. Notably, post-dyeing silver nanoparticle functionalization imparted pronounced and durable antimicrobial activity while preserving chromatic performance, demonstrating a scalable molecular platform that integrates high-performance coloration and hygienic functionality within a single textile dyeing system.

© 2026 by the authors; licensee Growing Science, Canada.

## 1. Introduction

The continuous convergence of textile chemistry with nanotechnology and biomedical materials science has transformed the conceptual framework of dye development. Modern colorants are no longer designed solely to impart aesthetic coloration but are increasingly engineered as multifunctional molecular systems capable of simultaneously providing chromatic performance, durability, and biological functionality.<sup>1-3</sup> Within this evolving technological landscape, azo dyes remain the most extensively utilized class of industrial colorants due to their synthetic versatility, structural tunability, and excellent fastness across a wide range of textile substrates.<sup>4</sup> Nevertheless, the rapidly advancing textile sector now demands dye systems that extend beyond simple coloration, incorporating additional functional attributes such as antimicrobial activity, environmental compatibility, and long-term performance stability.

Recent advances in synthetic chemistry have highlighted the pivotal role of five-membered nitrogen-containing heterocycles as highly versatile building blocks for the construction of modern functional materials and molecular systems. Owing to their unique electronic structures and structural diversity, these heterocyclic frameworks provide powerful platforms for the rational design of advanced molecules with tunable physicochemical and biological properties. Contemporary reviews have underscored the expanding importance of such heterocycles across multiple research fields, including medicinal chemistry, materials science, and functional dye development, largely due to their ability to support extended  $\pi$ -conjugation, facilitate electronic modulation, and accommodate diverse functionalization strategies.<sup>5,6</sup> Among these heterocyclic systems, pyrano[2,3-*c*]pyrazole derivatives have emerged as particularly attractive scaffolds for the development of advanced chromophoric architectures. Pyrano[2,3-*c*]pyrazole-based azo dyes represent a distinctive class of heterocyclic chromophores characterized by favorable electronic configurations, pronounced structural stability, and

\* Corresponding author

E-mail address [fatmaali1811@gmail.com](mailto:fatmaali1811@gmail.com) (F. A. Mohamed) [Drmoh.gamal@science.menofia.edu.eg](mailto:Drmoh.gamal@science.menofia.edu.eg) (M. G. Abouelenein)

© 2026 by the authors; licensee Growing Science, Canada

doi: 10.5267/j.ccl.2026.3.002

efficient charge delocalization throughout the heteroaromatic framework, which collectively promote extended  $\pi$ -conjugation and enhanced optical performance. These intrinsic features, together with their notable thermal and photochemical stability, render such systems promising candidates for the design of high-performance functional dyes.<sup>7,8</sup> Moreover, the deliberate incorporation of functional substituents such as  $\text{NH}_2$ ,  $\text{OH}$ , and  $\text{CN}$  groups allows precise modulation of electron distribution and intermolecular interactions, thereby strengthening dye–fiber affinity and improving fixation behavior within textile substrates.<sup>9</sup> When incorporated into monoazo or bisazo chromophoric systems, pyrano[2,3-*c*]pyrazole derivatives exhibit tunable absorption properties and strong interactions with fiber matrices, enabling efficient coloration even under demanding high-temperature dyeing conditions and supporting their potential application in advanced multifunctional textile systems.<sup>10,11</sup>

In addition to molecular chromophore design, the integration of nanotechnology into textile finishing has emerged as an innovative strategy for expanding the functional scope of dyed fabrics. Metallic and metal oxide nanoparticles such as silver (Ag), zinc oxide (ZnO), and titanium dioxide ( $\text{TiO}_2$ ) have proven to be effective auxiliaries in this domain, improving dye dispersion stability, preventing aggregation, and promoting better exhaustion and diffusion within fiber matrices.<sup>12–14</sup> The resulting dye–nanoparticle hybrid systems exhibit superior color depth, enhanced fastness to washing and light, and increased resistance to mechanical and thermal stresses.<sup>15,16</sup> Particularly noteworthy is the antimicrobial activity imparted by silver nanoparticles, which transforms dyed textiles into bioactive surfaces that inhibit microbial growth—a feature of increasing relevance in medical textiles, sportswear, personal protective equipment, and hygienic apparel.<sup>17–20</sup>

From a molecular interaction standpoint, the fusion of pyrano[2,3-*c*]pyrazole-based azo dyes with nanoparticle-based finishing strategies enables a synergistic effect, involving electrostatic interactions, surface adsorption, and chemical anchoring at the fiber interface. These interactions not only improve dye fixation and durability but also amplify the antibacterial efficacy, without compromising fabric integrity or wearer comfort. As a result, these hybrid approaches offer an exciting pathway toward dual-functional textiles that seamlessly combine aesthetic performance with protective bioactivity. A deeper understanding of dye–fiber and dye–nanoparticle interactions is thus essential for optimizing textile performance while meeting the demands of modern regulatory, sustainability, and safety standards.<sup>21,22</sup>

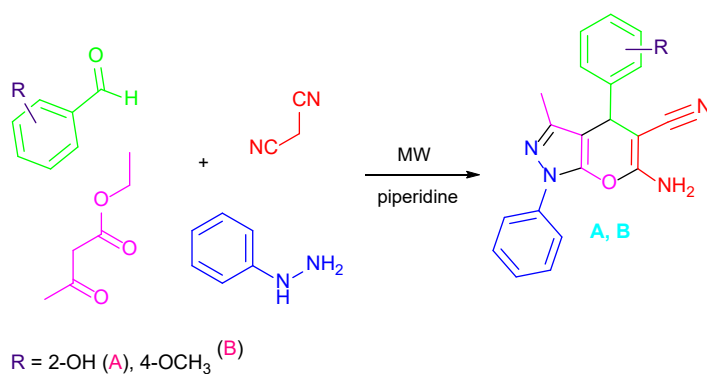
Despite these advancements, the integration of pyrano[2,3-*c*]pyrazole azo chromophores with eco-friendly one-pot synthetic strategies and post-dyeing silver nanoparticle functionalization remains largely unexplored. Particularly, studies that unify sustainable synthesis, high-performance dyeing, and durable antimicrobial finishing within a single scalable dyeing process are scarce.

This study, therefore, reports the rational design and green one-pot synthesis of a novel class of pyrano[2,3-*c*]pyrazole-based monoazo dyes, followed by comprehensive structural characterization using FT-IR, NMR, GC–MS, and elemental analysis. The dyeing performance of these dyes was systematically evaluated on polyester, nylon, and wool fabrics under high-temperature dyeing conditions, both before and after post-dyeing silver nanoparticle treatment. Furthermore, the antibacterial properties of the functionalized fabrics were assessed to determine their potential for advanced hygienic and biomedical textile applications. Through this integrated molecular and processing framework, the study paves the way for the development of sustainable, high-performance textile dyes that cater to both industrial performance and emerging biomedical needs.

## 2. Results and Discussion

### 2.1. Chemistry

A green and operationally efficient synthetic route was successfully established to construct structurally advanced pyrano[2,3-*c*]pyrazole frameworks suitable for subsequent functionalization. Specifically, a one-pot four-component condensation involving phenylhydrazine, ethyl acetoacetate, malononitrile, and either 2-hydroxybenzaldehyde or 4-methoxybenzaldehyde was carried out in ethanol using piperidine as a dual-function catalyst and base (**Scheme 1**).



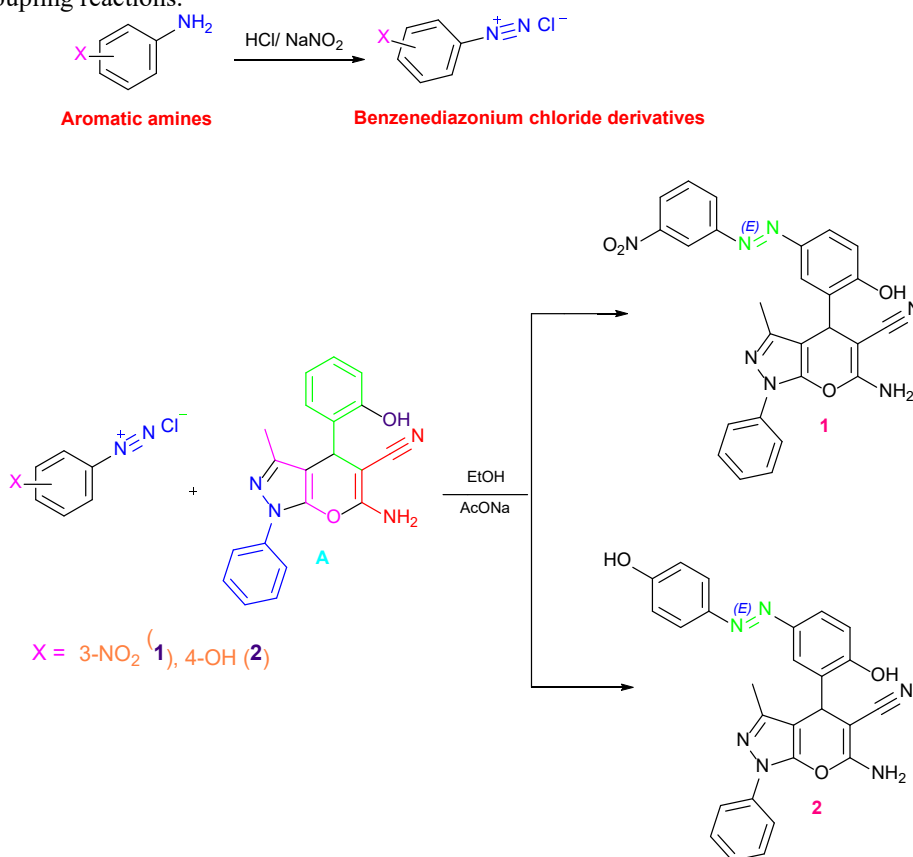
**Scheme 1.** Synthetic pathway of pyrano[2,3-*c*]pyrazole couplers (A, B).

This approach resulted in rapid molecular assembly with excellent atom economy and minimal purification requirements, demonstrating its compatibility with sustainable synthesis principles. The reaction pathway proceeds through sequential pyrazolone formation, Knoevenagel condensation, nucleophilic addition, and intramolecular cyclization, leading efficiently to the formation of 1,4-dihydropyrano[2,3-*c*]pyrazole-5-carbonitrile scaffolds. The resulting intermediates, designated **A** and **B**, were isolated in high purity and served as versatile coupling components for azo dye construction. The presence of either a 2-hydroxyphenyl moiety (**A**) or a 4-methoxyphenyl group (**B**) was deliberately introduced to modulate electronic density and reactivity during the subsequent diazo-coupling step.

The successful formation and high structural fidelity of intermediates **A** and **B** were confirmed through comprehensive spectroscopic and analytical characterization. FT-IR spectra revealed intense nitrile stretching vibrations at 2193  $\text{cm}^{-1}$  for **A** and 2191  $\text{cm}^{-1}$  for **B**, confirming the incorporation of the cyano functionality critical for electronic conjugation. The appearance of  $\text{NH}_2$  stretching bands in the range 3352–3427  $\text{cm}^{-1}$  and 3289–3357  $\text{cm}^{-1}$  further supported the formation of the aminopyrazole framework. Compound **A** exhibited an additional broad absorption at 3427  $\text{cm}^{-1}$  attributable to phenolic OH stretching, whereas compound **B** displayed a characteristic methoxy C–O stretching band at 1173  $\text{cm}^{-1}$ , reflecting the distinct substituent environments. The consistent observation of pyrazole C=N stretching at 1646–1648  $\text{cm}^{-1}$  and aromatic C=C vibrations near 1609–1612  $\text{cm}^{-1}$  indicates the establishment of an extended conjugated system, which is essential for subsequent chromophoric behavior.

$^1\text{H}$  NMR spectroscopy provided further insight into the molecular architecture of the synthesized intermediates. In compound **A**, a downfield singlet at  $\delta$  9.58 ppm was assigned to the phenolic OH proton, indicating intramolecular hydrogen bonding effects, while a singlet at  $\delta$  6.85 ppm corresponded to the  $\text{NH}_2$  group. The pyran  $\text{C}_4$ –H proton appeared as a singlet at  $\delta$  4.87 ppm, consistent with the rigid heterocyclic environment, and aromatic resonances were observed between  $\delta$  6.94 and 7.81 ppm. In compound **B**, the methoxy substituent resonated at  $\delta$  3.86 ppm, accompanied by analogous  $\text{NH}_2$ ,  $\text{C}_4$ –H, and methyl signals, together with a para-substituted aromatic pattern. The  $^{13}\text{C}$  NMR spectra corroborated these assignments, showing nitrile carbons near  $\delta$  117 ppm, quaternary  $\text{C}_5$  carbons adjacent to CN at  $\delta$  59–60 ppm, pyran  $\text{C}_4$  carbons at  $\delta$  20–22 ppm, and methyl carbons around  $\delta$  10 ppm. The methoxy carbon of compound **B** appeared at  $\delta$  55.98 ppm. These spectral features collectively confirm the successful construction of the target pyrano[2,3-*c*]pyrazole skeletons.

Electron impact mass spectrometry further verified molecular integrity, with molecular ion peaks at  $m/z$  344.08 for compound **A** and  $m/z$  358.11 for compound **B**, closely matching calculated values. Elemental analysis results were in excellent agreement with theoretical compositions, collectively demonstrating the high purity and structural consistency of intermediates **A** and **B**. Such well-defined intermediates are essential for ensuring controlled regioselectivity during subsequent azo coupling reactions.



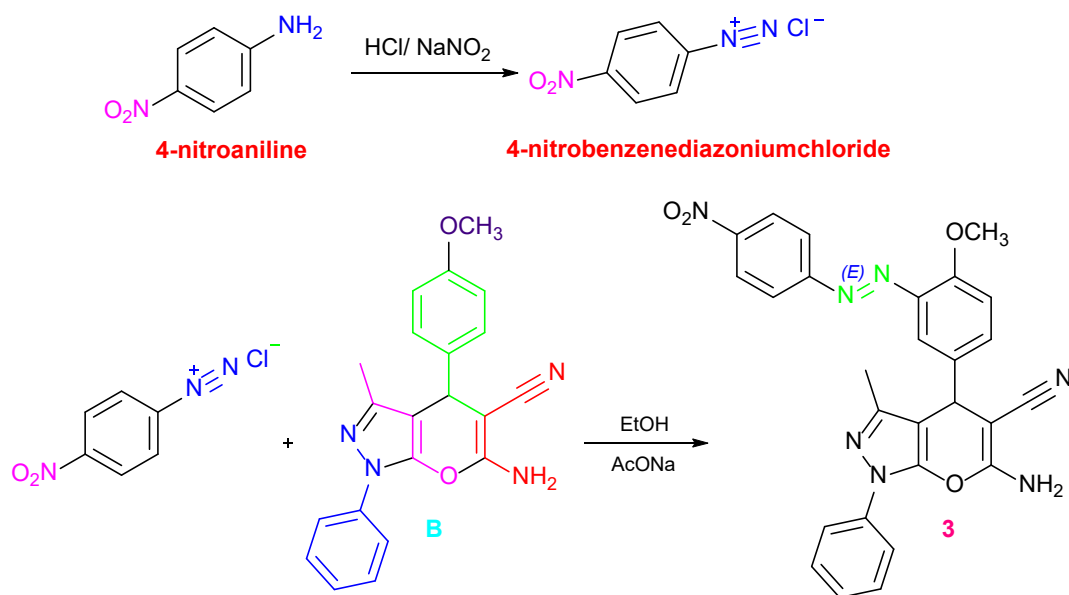
**Scheme 2.** Synthesis of pyrano[2,3-*c*]pyrazole-based monoazo disperse dyes (**1**, **2**)

The monoazo disperse dyes **1** and **2** were synthesized via regioselective diazotization–coupling reactions using compound **A** as the activated nucleophilic coupling partner (**Scheme 2**). In this process, aromatic amines were converted *in situ* into their corresponding diazonium salts under carefully controlled acidic conditions at low temperature, followed by coupling in buffered ethanolic medium. The use of sodium acetate maintained a mildly basic environment that favored electrophilic attack at the activated aromatic position of the pyrano[2,3-*c*]pyrazole core. This controlled reaction environment minimized side reactions and enabled selective C-coupling, resulting in structurally diverse monoazo chromophores featuring nitroaryl or bis-phenolic substituents that extend  $\pi$ -conjugation and modulate electronic distribution.

The formation of dyes **1** and **2** was confirmed by detailed spectroscopic analysis. In dye **1**, FT-IR spectra showed characteristic absorptions at 2205  $\text{cm}^{-1}$  (CN), 1650  $\text{cm}^{-1}$  (C=N), and 1515  $\text{cm}^{-1}$  corresponding to the azo linkage, together with distinct nitro group vibrations at 1525 and 1345  $\text{cm}^{-1}$ . The  $^1\text{H}$  NMR spectrum revealed a phenolic OH proton at  $\delta$  9.35 ppm,  $\text{NH}_2$  protons at  $\delta$  6.96 ppm, aromatic resonances spanning  $\delta$  7.55–8.94 ppm, a pyran  $\text{C}_4$ -H signal at  $\delta$  4.82 ppm, and a methyl resonance at  $\delta$  2.02 ppm. The  $^{13}\text{C}$  NMR data supported these assignments, with the nitrile carbon appearing at  $\delta$  120 ppm and pyran carbons at  $\delta$  59 and 23.1 ppm. The observed molecular ion peak at  $m/z$  493.19 closely matched the calculated value, and elemental analysis confirmed the proposed molecular formula.

Similarly, dye **2** exhibited FT-IR absorptions characteristic of phenolic OH groups at 3405 and 3228  $\text{cm}^{-1}$ , a nitrile band at 2206  $\text{cm}^{-1}$ , and an azo vibration at 1514  $\text{cm}^{-1}$ . The  $^1\text{H}$  NMR spectrum showed two phenolic OH signals at  $\delta$  9.85 and 9.2 ppm,  $\text{NH}_2$  protons at  $\delta$  6.81 ppm, and aromatic resonances between  $\delta$  7.4 and 8.79 ppm, consistent with a bis-phenolic azo structure. The  $^{13}\text{C}$  NMR spectrum confirmed the presence of the nitrile carbon at  $\delta$  118.1 ppm and pyran  $\text{C}_4$  at  $\delta$  22.9 ppm. The molecular ion peak at  $m/z$  464.2 and the elemental analysis data conclusively validated the successful synthesis and high compositional integrity of dye **2**.

Dye **3** was synthesized following a similar diazotization–coupling strategy, using compound **B** as the coupling component and 4-nitroaniline as the diazonium precursor (**Scheme 3**). The reaction proceeded smoothly, affording the target monoazo dye in 78% yield as a deeply colored caramel powder, indicative of efficient chromophore formation and extended conjugation.



**Scheme 3.** Synthesis of (*E*)-6-amino-4-(4-methoxy-3-((4-nitrophenyl)diazenyl)phenyl)-3-methyl-1-phenyl-1,4-dihydropyrano[2,3-*c*]pyrazole-5-carbonitrile (**3**).

The structure of dye **3** was confirmed by combined spectroscopic techniques. FT-IR analysis revealed  $\text{NH}_2$  stretching bands at 3380 and 3305  $\text{cm}^{-1}$ , a nitrile absorption at 2204  $\text{cm}^{-1}$ , C=N and aromatic C=C vibrations at 1651, 1603, and 1582  $\text{cm}^{-1}$ , a characteristic azo band at 1515  $\text{cm}^{-1}$ , nitro group absorptions at 1528 and 1344  $\text{cm}^{-1}$ , and a methoxy C–O–CH<sub>3</sub> vibration at 1248  $\text{cm}^{-1}$ . The  $^1\text{H}$  NMR spectrum displayed aromatic protons between  $\delta$  7.4 and 8.8 ppm,  $\text{NH}_2$  protons at  $\delta$  6.81 ppm, a pyran  $\text{C}_4$ -H signal at  $\delta$  4.74 ppm, a methoxy resonance at  $\delta$  3.83 ppm, and a methyl signal at  $\delta$  1.93 ppm. The  $^{13}\text{C}$  NMR spectrum further confirmed the molecular structure, with the nitrile carbon at  $\delta$  120.95 ppm, pyran  $\text{C}_4$  at  $\delta$  23.63 ppm, and methoxy carbon at  $\delta$  59.55 ppm. The molecular ion peak at  $m/z$  507.18 was in excellent agreement with the calculated value, and elemental analysis results closely matched theoretical predictions. Collectively, these data conclusively demonstrate the successful synthesis, structural integrity, and high purity of dye **3**.

Based on the well-established thermodynamic preference of azo compounds for the trans configuration, together with the observed spectroscopic characteristics and literature precedents, the synthesized azo dyes were assigned the thermodynamically favored *E* configuration.<sup>23-26</sup>

## 2.2. Dyeing of Wool Fabric

### 2.2.1. Effect of Concentration

A systematic shade build-up study was conducted for disperse dyes 1–3 at 1%, 2%, and 3% (pH 4, 100 °C, 1 h) in a water bath without dispersing agents. As shown in **Fig. 1**, all dyes produced measurable exhaustion and total fixation across the investigated shade range, with dye uptake trends that are consistent with practical disperse dyeing behavior on wool. Notably, Dye 2 delivered relatively higher exhaustion and total fixation than dyes 1 and 3 at all concentrations, indicating a more favorable dye–fiber interaction profile under the applied conditions. This advantage can be rationalized by the hydroxyl substituent in Dye 2, which increases polarity and enables additional intermolecular interactions (particularly hydrogen bonding) with the protein matrix, thereby promoting deeper diffusion and stronger retention within wool.

Across the three shade levels, the 1% concentration afforded the most efficient uptake (highest exhaustion and fixation). This outcome is typical of systems where fiber binding sites are not saturated and dye molecules remain better dispersed in the bath, maximizing the fraction of “dye available for transport.” At higher concentrations (2–3%), dye aggregation becomes more likely and the effective availability of diffusible dye decreases; consequently, the exhaustion efficiency becomes comparatively lower, despite the higher absolute amount of dye present. From an application standpoint, this concentration-response behavior supports the practical utility of the dyes, because high uptake at lower shade levels is generally desirable for cost-effective coloration.

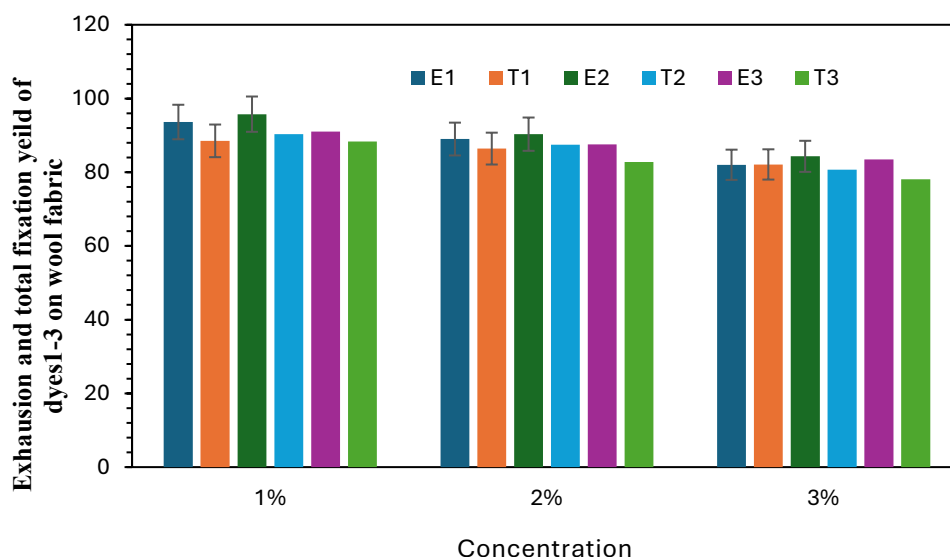


**Fig. 1.** Effect of exhaustion and total fixation yield of dyes 1–3 on wool at different concentrations at 100 °C for 1 h.

### 2.2.2. Effect of pH

The dyebath pH varied between pH 3 and 5 (100 °C, 1 h, no dispersing agent) to identify conditions that maximize dye uptake while maintaining bath and fiber stability. As illustrated in **Fig. 2**, pH 4 provided the most favorable balance, yielding the highest exhaustion and fixation for the tested dyes. At pH 3, excessive protonation of functional groups on wool can disrupt optimal dye–fiber interactions and reduce effective diffusion/anchoring, leading to notably lower uptake. At pH 5, the decreased acidity can compromise dispersion stability and promote aggregation, again lowering dye availability for fiber penetration and resulting in comparatively weaker exhaustion/fixation.

Within this pH window, Dye 2 consistently outperformed dyes 1 and 3, which is consistent with substituent-driven electronic effects: the electron-donating hydroxyl group increases electron density and interaction capability, whereas nitro-containing dyes (1 and 3) possess a more electron-withdrawing character that tends to weaken affinity toward the wool matrix under otherwise identical conditions. Importantly, the identification of pH 4 as an optimum aligns with operational expectations for dyeing efficiency and reproducibility, reinforcing the industrial relevance of the selected condition.

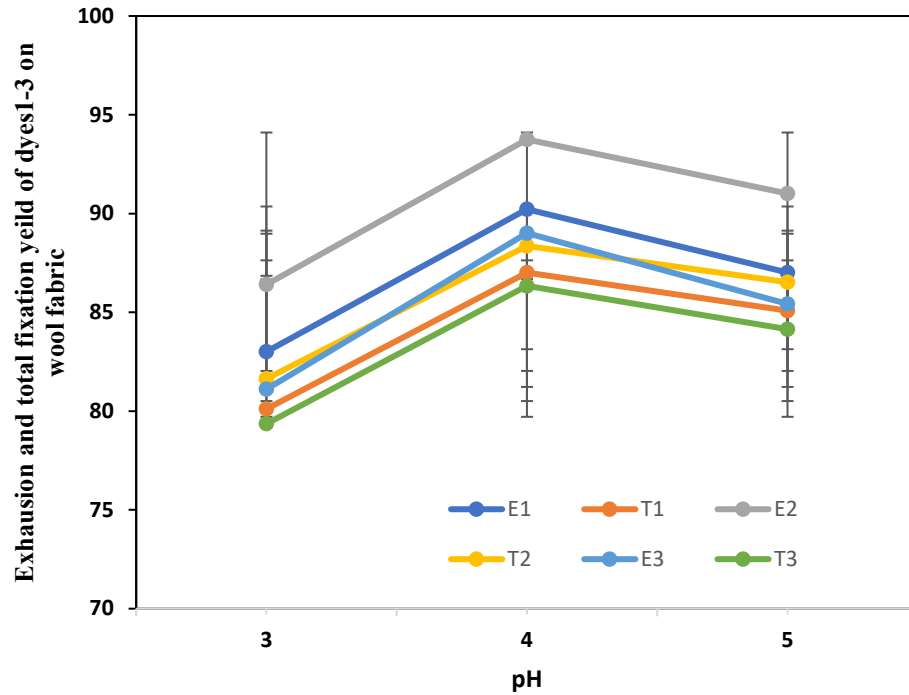


**Fig. 2.** Exhaustion and total fixation yield of dyes 1–3 on wool at 100 °C for 1 h at different pH values.

### 2.2.3. Effect of Temperature

The temperature dependence of dyeing was evaluated at 90 and 100 °C (pH 4, 1 h, no dispersing agent). As shown in **Fig. 3**, dyeing at 100 °C yielded markedly higher exhaustion and fixation for all dyes relative to 90 °C. This temperature-driven improvement can be attributed to enhanced dye mobility (higher kinetic energy) and increased fiber swelling/segmental mobility in the proteinaceous wool structure, which collectively accelerate diffusion and promote stronger dye–fiber association. From a processing perspective, 100 °C provides superior efficiency within a standard dyeing window, supporting the feasibility of adopting this condition without specialized auxiliaries.

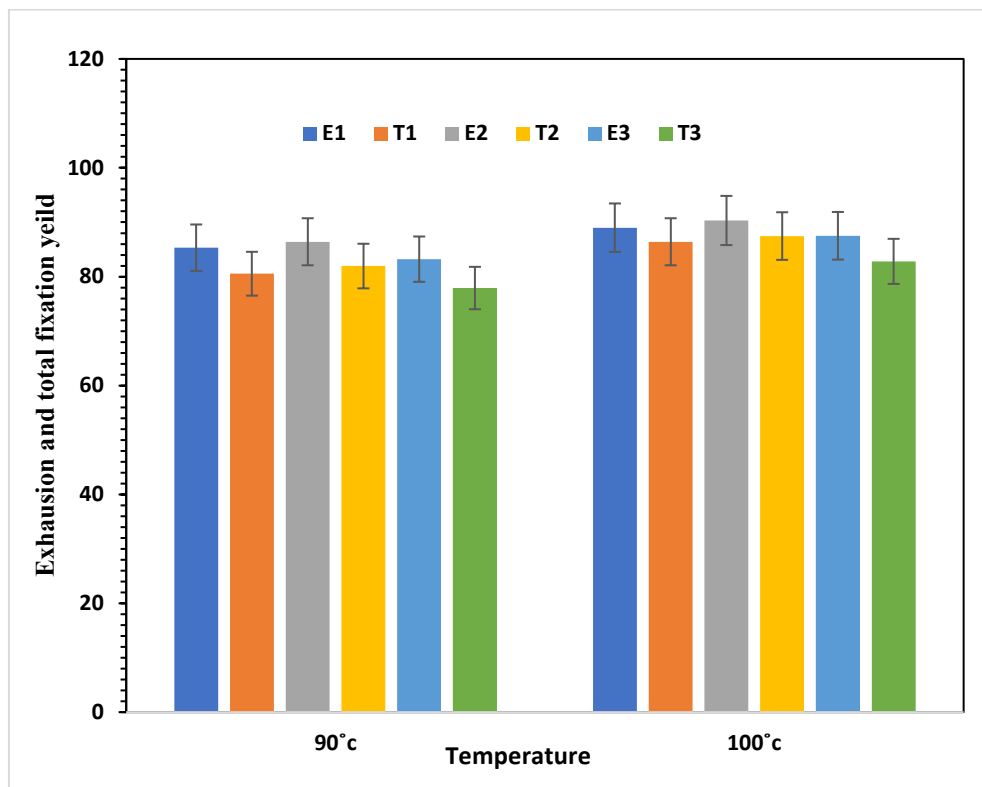


**Fig. 3.** Effect of exhaustion and total fixation yield of dyes 1–3 on wool at different temperatures at 2% shade and pH 4 for 1 h.

## 2.3. Dyeing of Polyester and Nylon Under High-Temperature High-Pressure Conditions

### 2.3.1. Effect of Concentration

The dyeing behavior of dyes 1–3 was examined at 1%, 2%, and 3% under HTHP conditions (pH 4, 110 °C, 1 h) without dispersing agents. As presented in **Figures 4** and **5**, all dyes achieved measurable uptake on both nylon and polyester, with performance patterns that are comparable to disperse dyeing expectations under high-temperature conditions. Across both substrates, Dye 2 again exhibited the highest exhaustion and total fixation, demonstrating a consistently stronger intrinsic affinity profile.

Mechanistically, the hydroxyl functionality in Dye 2 increases dye polarity and strengthens intermolecular interactions with fiber matrices, supporting more efficient diffusion and retention. In addition, the data indicates that the lowest shade concentration (1%) delivered the highest exhaustion efficiency, consistent with the availability of fiber binding sites and reduced bath aggregation at low loadings. As shade concentration increases, binding sites approach saturation and aggregation becomes more prominent, causing exhaustion efficiency to become relatively lower, even though deeper shades are obtained. This behavior is industrially meaningful because it reflects predictable shade build-up and highlights conditions where the dyes operate most efficiently.

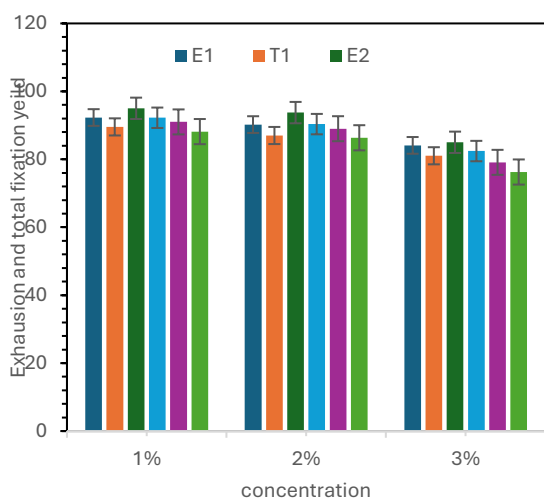


**Fig. 4.** Effect of concentration on exhaustion and total fixation yield of dyes 1–3 on nylon at pH 4 and 110 °C for 1 h.

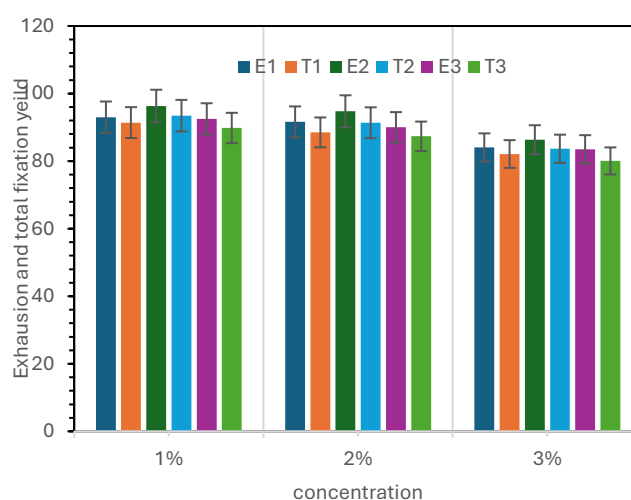


**Fig. 5.** Effect of concentration on exhaustion and total fixation yield of dyes 1–3 on polyester at pH 4 and 110 °C for 1 h.

### 2.3.2. Effect of pH

The influence of pH (3–5) on dyeing efficiency was evaluated for nylon and polyester at 110 °C for 1 h using an infrared dyeing machine without dispersing agents.

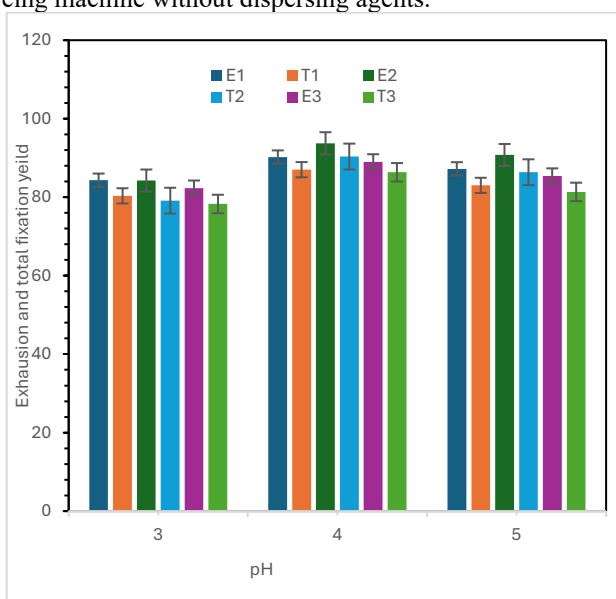


**Fig. 6.** Effect of pH on exhaustion and total fixation values of dyes 1–3 on nylon at 2% shade and 110 °C for 1 h.

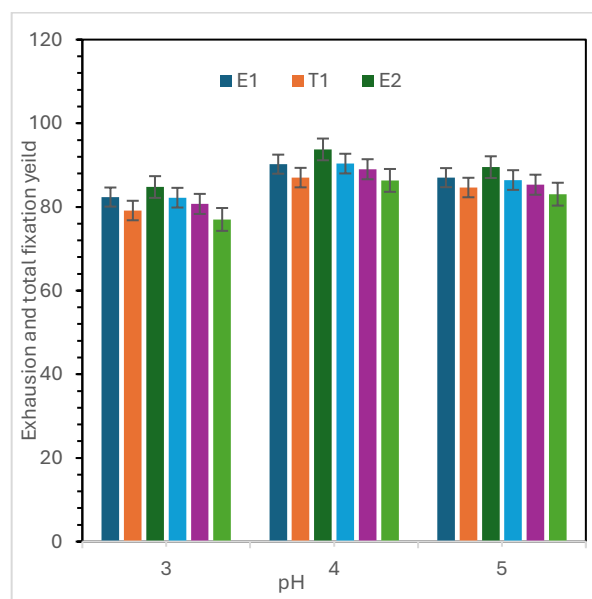


**Fig. 7.** Effect of pH on exhaustion and total fixation values of dyes 1–3 on polyester at 2% shade and 110 °C for 1 h.

As shown in **Fig. 6** and **Fig. 7**, pH 4 yielded the highest exhaustion and fixation for both fabrics, indicating that this pH offers the most favorable environment for dye stability and fiber interaction under high-temperature conditions. Accordingly, pH 4 was retained as the optimal operating condition for subsequent experiments, as it maximizes dyeing efficiency while maintaining bath and substrate stability, an important criterion for scale-up.

### 2.3.3. Effect of Temperature

The dyeing performance was further examined at 110 and 120 °C (pH 4, 1 h, no dispersing agent). The results in **Fig. 8** and **Fig. 9** show that increasing the temperature to 120 °C did not produce a meaningful improvement in exhaustion or fixation relative to 110 °C. Practically, this indicates that 110 °C offers comparable dyeing efficiency while providing clear operational advantages, lower energy demand, improved economic feasibility, and reduced thermal stress, without compromising uptake. This outcome supports 110 °C as a rational optimum for HTHP processing under the investigated conditions.

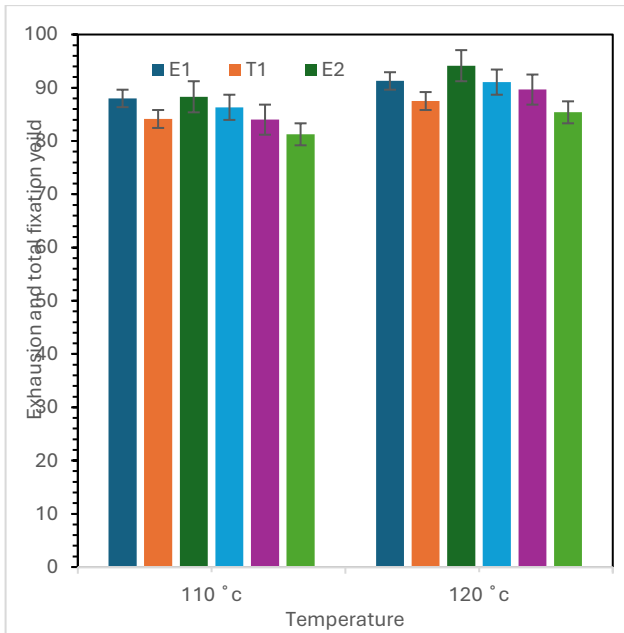


**Fig. 8.** Effect of temperature on exhaustion and total fixation values of dyes 1–3 on nylon at 2% shade and pH 4.

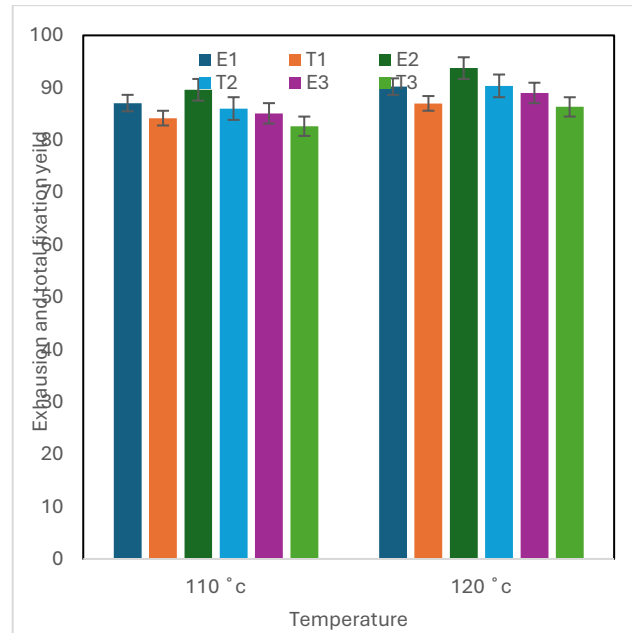


**Fig. 9.** Effect of temperature on exhaustion and total fixation values of dyes 1–3 on polyester at 2% shade and pH 4.

### 2.4. Nanosilver-Assisted Enhancement of Dye Exhaustion and Fixation on Wool, Nylon, and Polyester

The influence of nanosilver on dye exhaustion and total fixation was evaluated for dyes 1–3 on polyester and nylon (IR dyeing method) and on wool (conventional dyeing) at 2% shade and pH 4.

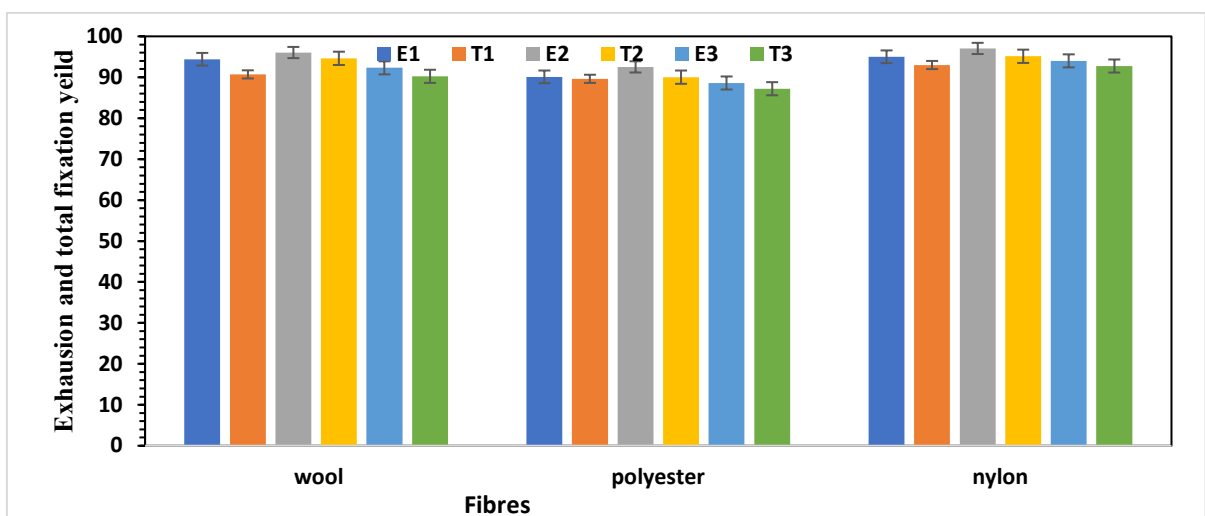


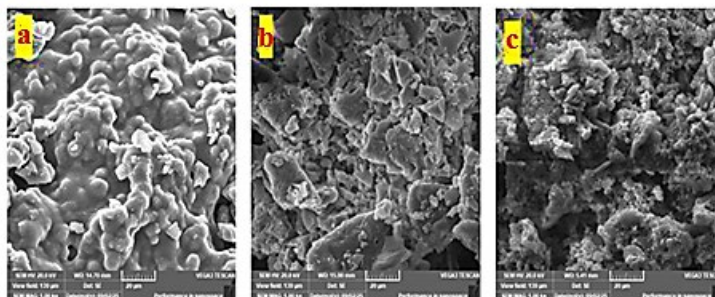
**Fig. 10.** Effect of nanosilver on exhaustion and total fixation values of dyed polyester, nylon, and wool fabrics at 2% shade and pH 4.

As shown in **Fig. 10**, nanosilver treatment led to a clear and practically meaningful increase in both exhaustion and fixation compared with nanoparticle-free dyeing. This improvement was observed across all substrates, indicating that nanosilver exerts a broadly beneficial interfacial effect rather than a fabric-specific anomaly. Among the dyes, dye **2** consistently achieved the highest exhaustion and fixation, consistent with its stronger intrinsic affinity toward the fiber matrices.

The enhancement associated with nanosilver can be explained by cooperative mechanisms that are well aligned with dyeing practice: improved dispersion stability (reducing aggregation), creation of additional adsorption/anchoring sites at the fiber interface, and intensified dye–fiber interactions that suppress back-diffusion during post-dyeing washing. The high surface area of nanosilver facilitates local dye enrichment near the fiber surface and promotes more efficient penetration into accessible microdomains, thereby increasing net uptake and fixation efficiency. From an application perspective, the nanosilver-assisted system provides a technologically attractive route to improve dyeing efficiency under dispersant-free conditions while simultaneously preparing fabrics for added functional performance.

### 2.5. SEM Analysis

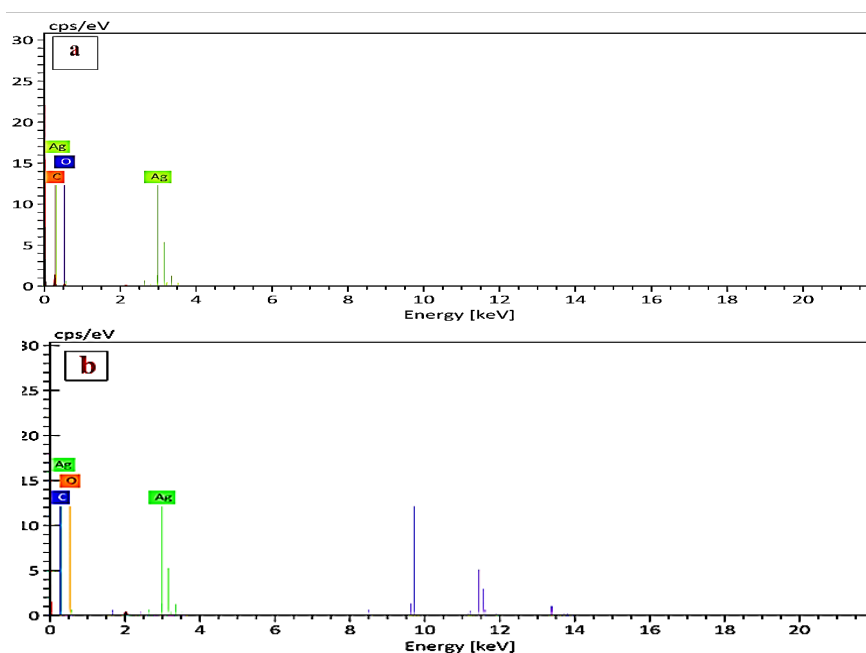
SEM micrographs shown in **Fig. 11** reveal three distinct surface morphologies arising from different processing conditions. Image **(a)**, corresponding to dye **1** displays relatively large, rounded aggregates with a cauliflower-like appearance, forming compact and fused domains that yield a smoother surface while maintaining moderate porosity. Image **(b)**, corresponding to dye **2** exhibits a heterogeneous morphology consisting of angular plate-like structures interspersed with smaller rounded domains, producing a more ordered architecture with discernible voids and reduced packing density. Image **(c)**, corresponding to dye **3** presents a highly porous sponge-like morphology characterized by an interconnected network of pores and channels resembling a foam or honeycomb structure. These observations confirm that processing conditions play a decisive role in governing nucleation and growth mechanisms, thereby dictating surface morphology and material performance.



**Fig. 11.** SEM micrographs showing the surface morphology of the samples prepared under different processing conditions at 1.00 kx magnification. Panels **(a)**–**(c)** correspond to the three representative samples. Scale bars represent 20  $\mu\text{m}$ .

### 2.6. EDX Analysis

The elemental compositions of the samples obtained under different processing conditions are illustrated in **Fig. 12**.



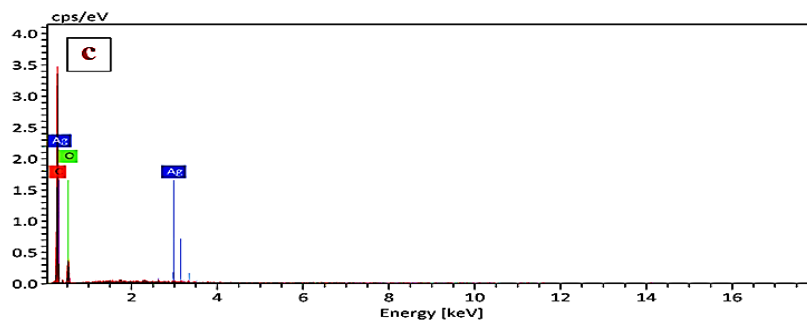


**Fig. 12.** EDX spectra showing elemental composition of the samples prepared under different processing conditions. Samples (a), (b), and (c) correspond to the SEM images shown in Fig. 11a, Fig. 11b, and Fig. 11c, respectively.

Sample (a) shows prominent Ag, O, and Cl peaks with varying intensities, indicating partial surface oxidation of silver and the presence of chloride species. The cauliflower-like morphology observed in SEM, together with this elemental profile, suggests the formation of a compact silver–chloride–oxide composite structure. Sample (b) also displays Ag, O, and Cl signals, together with minor additional peaks that may correspond to trace elements. The coexistence of angular and rounded morphologies reflects a heterogeneous elemental distribution, where oxygen is associated with oxide formation on crystalline silver domains and chlorine denotes residual chloride phases. Sample (c) exhibits the most distinct EDX profile, characterized by intense Ag peaks and altered O and Cl ratios relative to the other samples. The highly porous sponge-like structure correlates with increased surface exposure of silver and oxygen-containing species, indicating conditions favorable for applications requiring high surface reactivity. Overall, EDX analysis confirms that all samples are predominantly silver-based materials with varying degrees of oxidation and chloride incorporation, in agreement with the morphological diversity observed in SEM and their potential applicability in antimicrobial coatings and related functional systems.

### 2.7. Ultraviolet Protection Factor (UPF)

UPF values were interpreted according to AS/NZS 4399:1996, where higher UPF corresponds to stronger UV shielding and lower UVA/UVB transmittance indicates reduced penetration of harmful radiation. The effect of nanosilver finishing on UV protection was assessed by comparing UPF, UVA transmittance, and UVB transmittance for dyed fabrics before and after nano-treatment (Table 1). Overall, nanosilver finishing produced a notable improvement in UV protection for most samples, reflected by higher UPF values and reduced UVA/UVB transmission, demonstrating that the treatment contributes functional benefits beyond coloration.

**Table 1.** UPF data of dyed polyester and nylon fabrics processed by HTHP dyeing and dyed wool fabrics processed by conventional dyeing, with and without nanosilver treatment at 2% shade and pH 4.

No.	File Name*	AS/NZ S4399:1996 – UPF	AS/NZ S4399:1996 – UVA		AS/NZ S4399:1996 – UVB
			Transmittance		Transmittance
1	1n	14.1	2.5		7.9
2	1w	65.8	0.6		1.4
3	1p	107.3	0.5		1.0
4	2n	8.0	4.1		13.8
5	2w	3.2	24.7		29.3
6	2p	56.9	1.4		1.8
7	3n	13.0	1.6		8.2
8	3w	34.0	1.4		2.8
9	3p	62.9	0.7		1.7
10	1n nano	27.9	0.8		3.8
11	1w nano	56.4	1.0		1.6
12	1 p nano	111.5	0.4		1.0
13	2n nano	1.4	33.1		80.7
14	2w nano	76.5	0.8		1.1
15	2 p nano	58.9	2.2		1.5
16	3 n nano	0.8	39.7		134.6
17	3w nano	55.0	1.1		1.7
18	3 p nano	129.6	0.3		0.8

\*File Name denotes the coded identification of each tested sample. The number (1–3) corresponds to the dye number, whereas the letters n, w, and p represent nylon, wool, and polyester fabrics, respectively. Samples labeled “nano” indicate fabrics treated with silver nanoparticles (AgNPs) after dyeing.

For Sample 1, nylon showed a rise in UPF from 14.1 to 27.9 after nano-treatment, while polyester increased from 107.3 to 111.5, indicating an already high baseline UV performance for polyester that was further strengthened. In Sample 2, untreated fabrics exhibited weak UV protection (notably low UPF for nylon), whereas nano-treatment generated substantial functional gains, with wool and polyester reaching markedly higher UPF values and concomitantly reduced transmittance. Sample 3 also showed a clear enhancement after nano-treatment for wool and polyester, reaching excellent UV protection,

while nylon remained ineffective after treatment, highlighting that fabric architecture and intrinsic optical properties can dominate the final UPF outcome. In practical terms, nanosilver finishing appears more consistently effective for wool and polyester than for nylon in the current system, supporting the conclusion that functional finishing performance is substrate-dependent even under identical treatment conditions.

### 2.8. Colorimetric and Fastness Properties

The dyed fabrics exhibited very good to excellent fastness performance (**Table 2**), with rubbing and wash fastness values in the range of 4–5, indicating limited color change and minimal staining, levels that are within acceptable industrial ranges for commercial textile applications. Light fastness was also strong, and fabrics dyed in the presence of nanosilver showed notably improved light fastness relative to nanoparticle-free samples. This improvement can be attributed to nanosilver-mediated stabilization of dye distribution and stronger dye–fiber association, which reduce dye migration and surface enrichment, two factors that commonly exacerbate photodegradation.

**Table 2.** Fastness properties of polyester (P) and nylon (N) fabrics dyed under HTHP conditions and wool (W) fabrics dyed by conventional dyeing, using dyes with and without nanosilver treatment at 2% shade and pH 4.

Dye	Fabric	Fastness to rubbing		Wash fastness	Fastness to perspiration						
		Dry	Wet		Alkaline			Acidic			Light
Without nano	1P	4	4	4	4	4	4	4	4	4	
	1N	4	4	4	4	4	4	4	4	4	4
	1W	4	4	4	4	4	4	4	4	4	4
	2P	4-5	5	4-5	4-5	4-5	4-5	4-5	4-5	4-5	5
	2N	4-5	5	4-5	4-5	4-5	4-5	4-5	4-5	4-5	5
	2W	4-5	5	4-5	4-5	4-5	4-5	4-5	4-5	4-5	5
	3P	4	4	4	4	4	4	4	4	4	4
	3N	4	4	4	4	4	4	4	4	4	4
	3W	4	4	4	4	4	4	4	4	4	4
With nano	1P	4-5	4-5	4-5	4-5	4-5	4-5	4-5	4-5	4-5	5
	1N	4-5	4-5	4-5	4-5	4-5	4-5	4-5	4-5	4-5	5
	1W	4-5	4-5	4-5	4-5	4-5	4-5	4-5	4-5	4-5	5
	2P	4-5	4-5	4-5	4-5	4-5	4-5	4-5	4-5	4-5	5
	2N	4-5	4-5	4-5	4-5	4-5	4-5	4-5	4-5	4-5	5
	2W	4-5	4-5	4-5	4-5	4-5	4-5	4-5	4-5	4-5	5
	3P	4-5	4-5	4-5	4-5	4-5	4-5	4-5	4-5	4-5	5
	3N	4-5	4-5	4-5	4-5	4-5	4-5	4-5	4-5	4-5	5
	3W	4-5	4-5	4-5	4-5	4-5	4-5	4-5	4-5	4-5	5

**Table 3.** Colorimetric parameters of polyester (P) and nylon (N) fabrics dyed under high-temperature high-pressure conditions and wool (W) fabrics dyed by the conventional method at 2% shade and pH 4, with and without nanosilver finishing.

$\lambda$ max	Dye	Properties							
		Fabric	K/S	L*	a*	b*	C°	h°	dE*
Dye1 380	Without nano	1P	11.83	73.46	3.84	52.88	53.01	85.84	54.82
		1N	9.17	72.60	7.45	42.26	42.91	79.99	51.48
		1W	5.03	67.00	6.87	35.46	36.12	79.04	29.72
Dye 2 415		2P	12.45	57.86	12.13	52.98	54.35	77.10	61.18
		2N	8.31	63.74	13.19	54.94	56.50	76.50	67.13
		2W	19.01	53.36	20.38	54.10	57.81	69.36	55.93
Dye 3 375		3P	18.13	66.12	4.32	57.82	57.99	85.73	61.48
		3N	7.75	79.23	1.54	34.54	34.58	87.45	41.93
		3W	6.58	68.71	3.79	37.82	38.01	84.27	30.34
Dye1 380	With nano	1P	26.25	67.65	7.19	55.82	56.28	82.66	57.77
		1N	27.14	60.99	10.31	41.03	42.31	75.89	50.20
		1W	5.93	66.64	5.22	30.94	31.38	80.42	24.49
Dye 2 415		2P	7.61	64.42	8.56	52.51	53.20	80.74	55.71
		2N	13.89	44.95	13.03	41.31	43.31	72.50	58.21
		2W	5.62	62.34	11.53	44.52	45.99	75.48	39.67
Dye 3 375		3P	23.26	67.29	6.00	59.28	59.58	84.22	61.06
		3N	11.24	56.96	3.75	32.12	32.33	83.34	42.97
		3W	4.20	72.62	2.22	31.98	32.06	86.03	22.33

Color strength and CIE parameters (**Table 3**) further supported the dyeing trends, with the highest K/S values obtained at pH 4, consistent with the exhaustion/fixation results. In several cases, nanosilver treatment produced substantial gains in apparent color depth for synthetic substrates. For instance, polyester sample 1P increased from K/S = 11.83 to 26.25 after nano-treatment, and nylon sample 1N increased from 9.17 to 27.14, indicating that nanosilver finishing can markedly intensify color strength on hydrophobic fibers under the adopted conditions. Mechanistically, this behavior is consistent

with improved dispersion, increased interfacial adsorption, and enhanced retention of dye within near-surface microdomains—effects that are particularly impactful for polyester and nylon where diffusion/anchoring limitations are often more pronounced.

By contrast, wool exhibited only minor K/S changes after nano-treatment and, in some cases, slight decreases. This comparatively modest response is plausibly linked to the inherently higher density of active binding sites and stronger baseline dye–fiber interactions in wool, which reduces the relative contribution of nanosilver to uptake/retention. Overall, the data show that nanosilver finishing is especially effective for enhancing color strength on polyester and nylon, while wool already demonstrates strong baseline performance with a smaller incremental benefit from nano-treatment.

The parameters  $L^*$ ,  $a^*$ ,  $b^*$ ,  $C^*$ ,  $h^\circ$ , and  $\Delta E^*$  are used to quantitatively evaluate the color properties of dyed fabrics.  $L^*$  represents lightness,  $a^*$  and  $b^*$  describe the red–green and yellow–blue color coordinates, respectively,  $C^*$  indicates color saturation (chroma),  $h^\circ$  represents the hue angle, and  $\Delta E^*$  expresses the overall color difference between samples. These parameters give an objective method to evaluate color depth, shade variation, and color changes after dyeing or treatment.

### 2.9. Structure–Performance Interpretation (comparative, nano-enabled SAR)

The observed differences in dyeing performance among dyes 1–3 are consistent with substituent-controlled electronic effects and become more pronounced when nanosilver is introduced as an interfacial modifier. Hydroxyl-containing dyes exhibit relatively higher intrinsic exhaustion and fixation, consistent with increased interaction capability and stronger affinity toward polar functional groups in wool and nylon through hydrogen bonding and dipole–dipole interactions. In contrast, nitro-substituted dyes show comparatively lower baseline uptake, reflecting weaker intrinsic affinity under the same dyeing conditions.

Upon nanosilver incorporation, the system transitions from a purely molecular SAR to a hybrid nano-enabled SAR in which interfacial phenomena amplify structure–property relationships. Hydroxyl-substituted dyes are more likely to associate strongly with nanosilver through oxygen-containing functionalities, promoting stable dye–nanoparticle assemblies that can be efficiently immobilized at the fiber interface. This cooperative binding suppresses back-diffusion and enhances dye residence time during dyeing and washing, producing notably improved exhaustion, fixation, and K/S values. Nitro-substituted dyes, although weaker in coordination propensity, still benefit from improved interfacial distribution and dispersion stability, leading to moderate but consistent gains in uptake. Collectively, these outcomes show that nanosilver finishing does not merely increase dyeing metrics in an absolute sense; rather, it introduces a controllable nanoscale interfacial contribution that converts substituent-driven affinity differences into practically meaningful performance advantages, especially for polyester and nylon.

### 2.10. Antimicrobial Assessment

The antimicrobial activity of dyes 1–3 was assessed by the agar diffusion method, and inhibition zone diameters are summarized in **Table 4** and visualized in **Figure 13**. The tested panel comprised two bacteria (*Escherichia coli* and *Staphylococcus aureus*) and two fungi (*Candida albicans* and *Aspergillus niger*), enabling a direct comparison of antibacterial versus antifungal responses across structurally related dyes.

Under nanoparticle-free conditions, the three dyes displayed clearly observable antibacterial activity with a predominantly bacterial-selective profile, while no detectable inhibition was recorded against the two fungal strains (**Table 4**). Dye 1 showed a pronounced effect against *S. aureus* (21 mm) together with a measurable response against *E. coli* (15 mm), indicating a stronger activity trend toward Gram-positive bacteria under the present assay. Dye 2 produced moderate inhibition zones against *E. coli* (16 mm) and *S. aureus* (14 mm), suggesting a lower intrinsic antibacterial potency relative to dyes 1 and 3. Dye 3 exhibited a selective antibacterial pattern similar to dye 1, with inhibition zones of 21 mm against *S. aureus* and 14 mm against *E. coli*; notably, its response toward *S. aureus* was higher than that of dye 2 under identical conditions. Collectively, these results indicate that, in the absence of nanosilver, the dyed scaffolds alone provide a bacterial-directed activity signature, with *S. aureus* being the most responsive organism in this study.

**Table 4.** Antimicrobial activity of dyes 1–3 without nanosilver against the tested microorganisms.

Dye	Clear zone			
	<i>S. aureus</i>	<i>E. coli</i>	<i>C. albicans</i>	<i>A. niger</i>
1	21	15	0	0
2	14	16	0	0
3	21	14	0	0

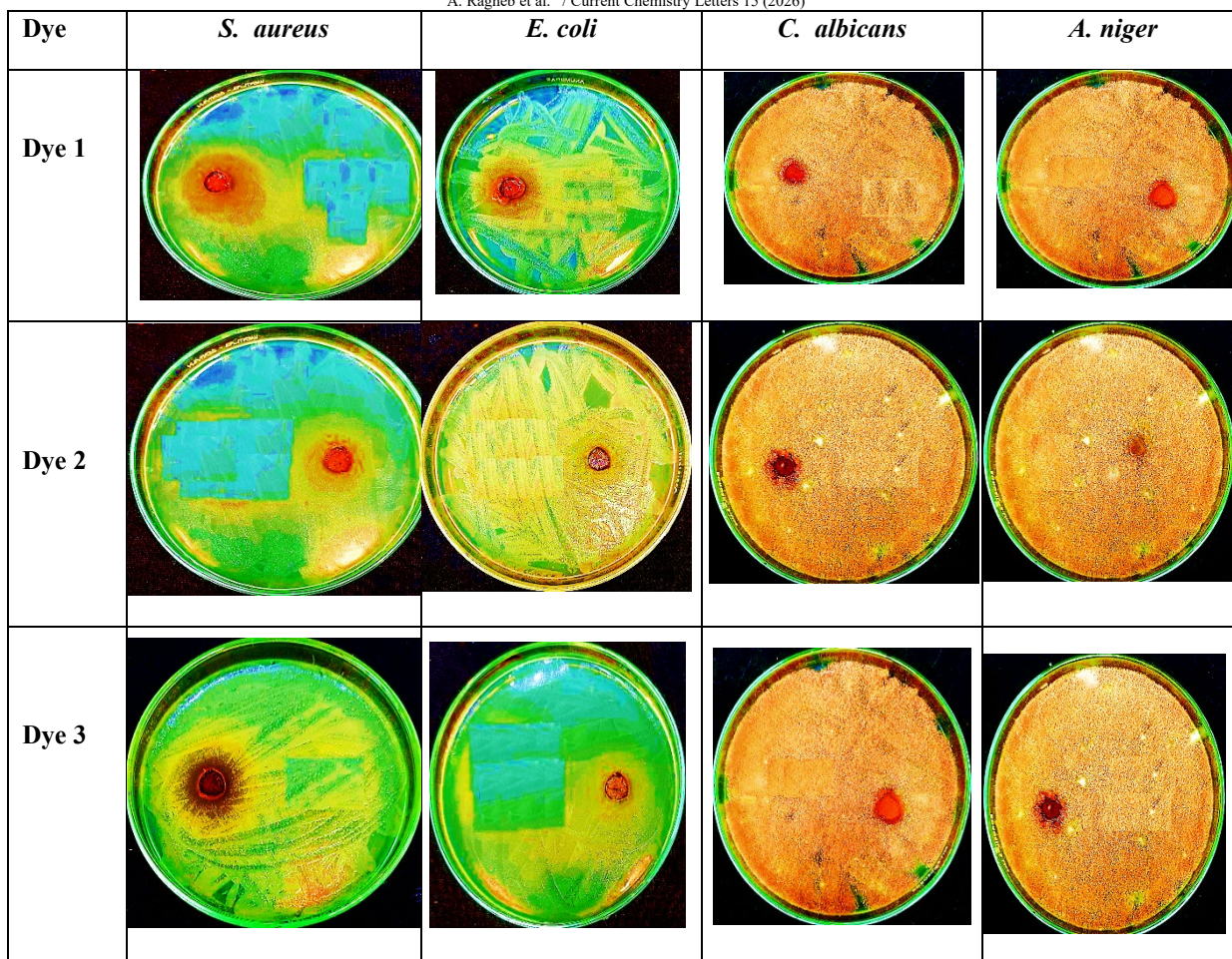


Fig. 13. Inhibition zone diameters (mm) of dyes 1–3 against *E. coli*, *S. aureus*, *C. albicans*, and *A. niger*.

### 2.10.1. Silver Nanoparticle–Mediated Enhancement of Antimicrobial Activity

Following nanosilver incorporation, inhibition zones increased in a marked and consistently measurable manner (Table 5; Fig. 14), confirming the functional contribution of AgNP finishing to antimicrobial performance. This enhancement is consistent with widely recognized AgNP actions at microbe–surface interfaces: nanosilver can interact strongly with microbial envelopes, increasing membrane permeability; it can also release Ag<sup>+</sup> ions that bind to thiol-containing proteins and enzymes, impairing essential metabolic functions; additionally, AgNP-associated reactive oxygen species can induce oxidative stress that damages lipids, proteins, and nucleic acids. In the present system, coupling AgNPs with the dye layer is expected to concentrate silver species at the textile surface, increasing the density of active antimicrobial sites and strengthening contact-mediated effects.

A comparison of the nanosilver-treated dyes reveals a shift from purely antibacterial selectivity to a broader spectrum that includes fungi (Table 5). Dyes 1 and 3 maintained strong antibacterial responses, particularly toward *S. aureus*, while also gaining measurable antifungal activity after nanosilver treatment. By contrast, dye 2 displayed the most apparent enhancement in antifungal performance, yielding the largest inhibition zones against *A. niger* and *C. albicans* among the three nanosilver-treated systems. This divergence in spectrum is consistent with substituent-controlled interfacial behavior: nitro-containing dyes (1 and 3) can favor stronger interactions with bacterial envelopes and promote contact-driven antibacterial effects, whereas hydroxyl-containing dye 2 may support more effective interfacial association and retention in environments relevant to fungal cell wall components through hydrogen-bonding and polarity-driven interactions. Importantly, these observations suggest that antimicrobial selectivity in the nano-finished textiles is not solely dictated by AgNPs but is also influenced by the chemical microenvironment established by the dye scaffold.

Table 5. Antimicrobial activity of dyes 1–3 after nanosilver treatment against the tested microorganisms.

Dye	Clear zone			
	<i>S. aureus</i>	<i>E. coli</i>	<i>C. albicans</i>	<i>A. niger</i>
1	21	17	15	14
2	16	15	20	21
3	20	20	16	15

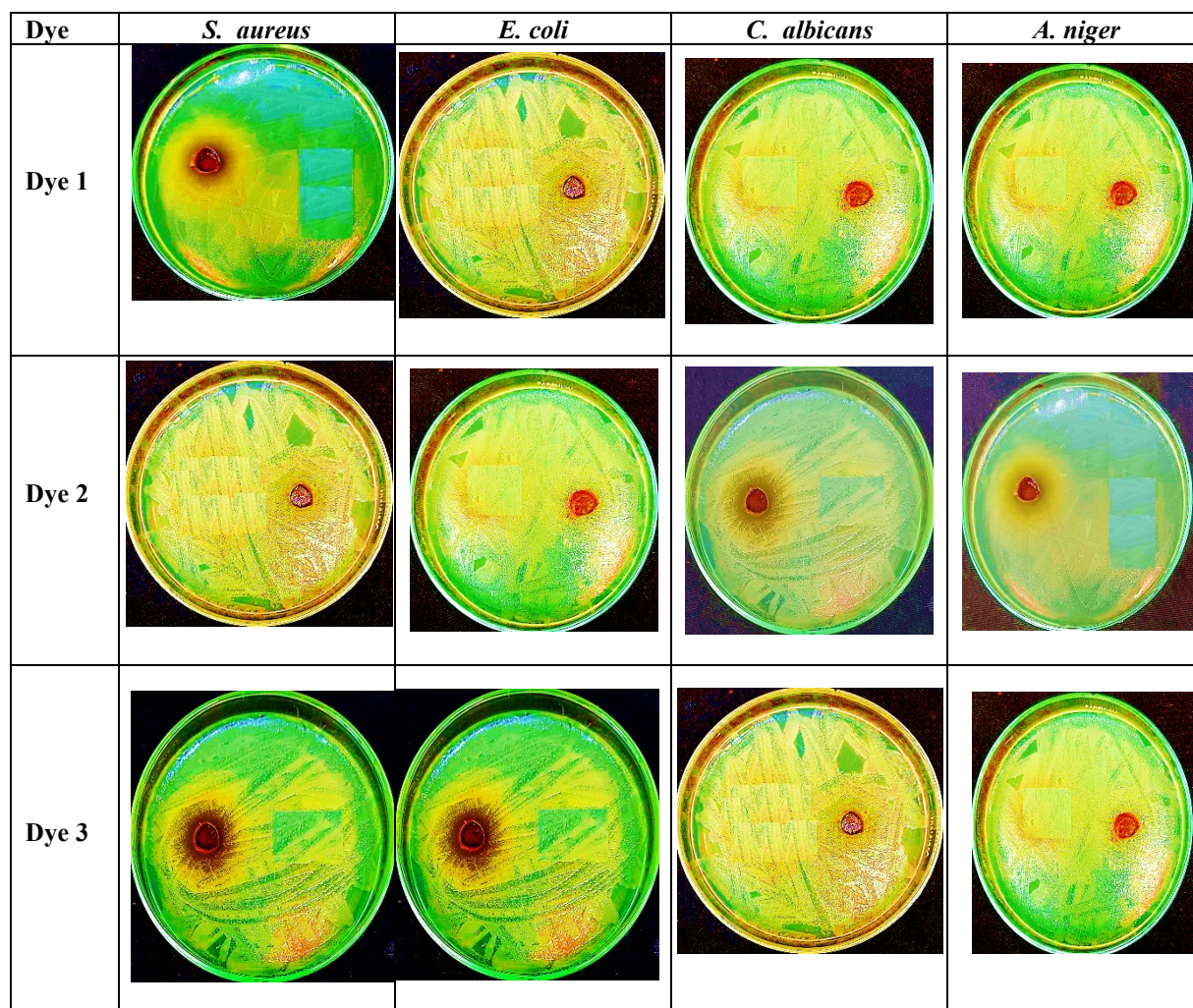


**Fig. 14.** Inhibition zone diameters (mm) of nanosilver-treated dyes 1–3 against *E. coli*, *S. aureus*, *C. albicans*, and *A. niger*.

### 2.10.2 Mechanistic Interpretation and Structure–Activity Context

Overall, the antimicrobial response of dyes 1–3 is governed by substituent chemistry in the baseline (nano-free) state and becomes substantially amplified once AgNPs are introduced. Nitro-substituted dyes tend to show stronger antibacterial responses, particularly toward Gram-positive bacteria, consistent with enhanced electrostatic interactions and membrane-associated perturbations under the present assay. In contrast, the hydroxyl-functionalized dye exhibits a comparatively broader tendency toward fungal inhibition after nanosilver treatment, plausibly due to polarity and hydrogen-bonding interactions that facilitate interfacial association with fungal cell wall constituents.

During nano-finishing, AgNPs are expected to be immobilized within the dye-coated surface layer through combined adsorption, electrostatic attraction, and coordination at heteroatom-rich sites. This produces a surface with a higher density of biologically active centers and increases the likelihood of sustained contact between microbial cells and silver-rich domains. Upon contact, the AgNP-containing interface can induce membrane deformation and permeability loss, while Ag<sup>+</sup> release and oxidative stress pathways contribute to enzyme inactivation and macromolecular damage. The dye scaffold plays a complementary role by governing nanoparticle spatial distribution and maintaining nanosilver proximity at the fiber–microbe interface, thereby translating molecular substituent effects into clearly observable differences in antimicrobial spectrum and intensity. Collectively, these findings support a tunable, nano-enabled antimicrobial textile platform in which substituent chemistry influences both baseline activity and the biological outcome of AgNP finishing.

### 3. Conclusions

This study establishes an integrated molecular–processing platform in which pyrano[2,3-*c*]pyrazole monoazo dyes function beyond conventional coloration, serving simultaneously as chromophores and interfacial functional agents for advanced textiles. By combining a green one-pot multicomponent synthesis with controlled diazo coupling, structurally tunable dyes were obtained that bridge sustainable chemistry with performance-driven textile engineering.

A key contribution of this work lies in demonstrating how subtle substituent modulation within the pyrano[2,3-*c*]pyrazole framework governs not only chromophoric behavior but also interfacial interactions with fibers and nanoscale modifiers. This structure-guided approach clarifies how molecular electronics translate into predictable dyeing efficiency, fixation behavior, and functional responsiveness across chemically distinct substrates, including wool, nylon, and polyester.

Importantly, post-dyeing silver nanoparticle finishing transforms the dyes from passive colorants into active surface architecture. Rather than acting as an additive effect alone, nanosilver introduces a nano-enabled structure–activity relationship in which dye chemistry directs nanoparticle anchoring, spatial distribution, and biological selectivity. This hybridization rationally couples color depth, ultraviolet attenuation, and antimicrobial performance within a single dyeing sequence, without reliance on auxiliary fixation or post-processing complexity.

According to the findings, fabrics treated with nanoparticles showed noticeably higher colour strength (K/S values) than untreated samples, suggesting better dye uptake and fixing. For every fiber under investigation, the ideal dyeing conditions were reached at pH 4. Wool performed best at 100 °C to prevent fiber breakdown, whereas higher temperatures (110 °C) improved colour diffusion for polyester and nylon.

In general, the dyed fabrics' fastness qualities were very good to excellent, especially when it came to washing, rubbing, and sweating. Additionally, light fastness was adequate, particularly for wool and polyester textiles. The use of nanoparticles enhanced the colored fabrics' antibacterial activity, durability, and colour consistency.

From an application perspective, the presented system offers a scalable and environmentally aligned route toward multifunctional textiles where coloration, protection, and durability are intrinsically linked at the molecular and interfacial levels. The design principles outlined here provide a foundation for future expansion toward smart and hygienic textile platforms, including medical fabrics, protective garments, and performance apparel, where sustainable synthesis and multifunctionality are increasingly essential.

## 4. Experimental

### 4.1. Materials and Fabrics

*Staphylococcus aureus* ATCC 6538-P and *Escherichia coli* ATCC 25933 were employed as representative Gram-positive and Gram-negative bacterial strains, respectively. Three mill-scoured and bleached textile substrates, namely wool (W), polyester (PET), and nylon, were supplied by Misr El-Mahala Co., Egypt. The wool fabric (210 g m<sup>-2</sup>) was woven in a 2/2 twill pattern with a thread density of 26 × 24 threads cm<sup>-1</sup>. Polyester fabric (149 g m<sup>-2</sup>) consisted of continuous filament plain weave, whereas the nylon fabric (149 g m<sup>-2</sup>) showed comparable structural features.

Prior to dyeing, all fabrics were purified to remove residual impurities. The substrates were treated in an aqueous bath containing 5 g L<sup>-1</sup> non-ionic detergent (Hostapal CV, Clariant-Egypt) and 2 g L<sup>-1</sup> sodium carbonate at a liquor ratio of 50:1. The treatment was conducted at 60 °C for 30 min, followed by thorough rinsing with distilled water and air-drying at room temperature.

### 4.2. Preparation of Silver Nanoparticles (AgNPs)

A 0.01 M aqueous solution of AgNO<sub>3</sub> was added to a solution of poly(vinyl alcohol) (PVA, 3 g per 100 mL) containing glucose (0.15 g per 100 mL), which acted as an antioxidant in all experiments. The reduction reaction was allowed to proceed at room temperature for 72 h.<sup>27</sup>

### 4.3. Chemistry

Melting points were determined using a Kofler block apparatus and are reported uncorrected. FT-IR spectra were recorded on a Thermo Fisher Scientific spectrophotometer using KBr pellets and are expressed in cm<sup>-1</sup>. <sup>1</sup>H and <sup>13</sup>C NMR spectra were obtained on a JEOL spectrometer operating at 500 and 125 MHz, respectively, using TMS as internal standard and DMSO-*d*<sub>6</sub> as solvent. Mass spectra were measured using a Shimadzu GC-MS instrument operating at 70 eV. Reaction progress was monitored by TLC on silica gel 60 F<sub>254</sub> aluminium plates.

#### 4.3.1. General Procedure for the Synthesis of Pyrano[2,3-*c*]pyrazole Congeners (**A**, **B**)

The β-enaminonitrile intermediates **A** and **B** were prepared *via* condensation of phenylhydrazine, ethyl acetoacetate, malononitrile, and either 2-hydroxybenzaldehyde (**A**) or 4-methoxybenzaldehyde (**B**) following the reported method.<sup>7–10</sup>

#### 4.3.1.1. 6-amino-4-(2-hydroxyphenyl)-3-methyl-1-phenyl-1,4-dihydropyrano[2,3-*c*]pyrazole-5-carbonitrile (**A**)

White powder; Yield 94%; mp: 244-246 °C; IR (KBr)  $\text{cm}^{-1}$  $\nu_{\text{max}}$ : 3427, 3352 (NH<sub>2</sub>), 3046, 2933, 2193 (CN), 1648 (C=N), 1612 (C=C); <sup>1</sup>H NMR (500 MHz, DMSO-*d*<sub>6</sub>)  $\delta$  (ppm): 9.58 (br.s, 1H, OH), 6.94-7.81 (m, 9H, Ar-H), 6.85 (s, 2H, NH<sub>2</sub>), 4.87 (s, 1H, C<sub>4</sub>-H (pyran)), 1.98 (s, 3H, CH<sub>3</sub>); <sup>13</sup>C NMR (125 MHz, DMSO-*d*<sub>6</sub>)  $\delta$  (ppm): 164.25 (C<sub>6</sub>-NH<sub>2</sub>), 159.31, 153.87, 147.09, 137.24, 130.52, 130.14 (2C), 127.43, 126.46, 123.07 (2C), 121.24, 119.48, 117.08 (CN), 115.76, 113.46 (C<sub>3</sub>-CH<sub>3</sub>), 59.46 (C<sub>5</sub>-CN), 20.46 (C<sub>4</sub>, pyran), 10.09 (CH<sub>3</sub>); EIMS, *m/z* [M]<sup>+</sup> calcd: 344.13; found: 344.08; Elemental Analysis for C<sub>20</sub>H<sub>16</sub>N<sub>4</sub>O<sub>2</sub> (%), Calcd: C, 69.76; H, 4.68; N, 16.27; found: C, 69.72; H, 4.64; N, 16.22.

#### 4.3.1.2. 6-amino-4-(4-methoxyphenyl)-3-methyl-1-phenyl-1,4-dihydropyrano[2,3-*c*]pyrazole-5-carbonitrile (**B**)

White powder; Yield 93%; mp: 246-248 °C; IR (KBr)  $\text{cm}^{-1}$  $\nu_{\text{max}}$ : 3357, 3289 (NH<sub>2</sub>), 3053, 2939, 2927, 2191 (CN), 1646 (C=N), 1609, 1173 (C-O); <sup>1</sup>H NMR (500 MHz, DMSO-*d*<sub>6</sub>)  $\delta$  (ppm): 7.9-7.92 (m, 5H, Ar-H), 7.43-7.45 (d, 2H, *J* = 9 Hz, Ar-H), 6.99-7.01 (d, 2H, *J* = 9 Hz, Ar-H), 6.89 (s, 2H, NH<sub>2</sub>), 4.89 (s, 1H, C<sub>4</sub>-H (pyran)), 3.86 (s, 3H, OCH<sub>3</sub>), 1.99 (s, 3H, CH<sub>3</sub>); <sup>13</sup>C NMR (125 MHz, DMSO-*d*<sub>6</sub>)  $\delta$  (ppm): 164.67 (C<sub>6</sub>-NH<sub>2</sub>), 159.58, 147.13, 137.27, 130.64, 130.24 (2C), 127.65 (2C), 126.61, 123.14 (2C), 121.34, 119.53, 117.27 (CN), 115.86, 113.74 (C<sub>3</sub>-CH<sub>3</sub>), 60.41 (C<sub>5</sub>-CN), 55.98 (OCH<sub>3</sub>), 21.78 (C<sub>4</sub>, pyran), 10.14 (CH<sub>3</sub>); EIMS, *m/z* [M]<sup>+</sup> calcd: 358.14; found: 358.11; Elemental Analysis for C<sub>21</sub>H<sub>18</sub>N<sub>4</sub>O<sub>2</sub> (%), Calcd: C, 70.38; H, 5.06; N, 15.63; found: C, 70.33; H, 5.02; N, 15.61.

#### 4.3.2. General Procedure for the Synthesis of 4-(2-hydroxyphenyl)-1,4-dihydropyrano[2,3-*c*]pyrazole Based Azo Disperse Dyes (**1,2**)

An ice-cold solution of the appropriate amine, namely 3-nitroaniline (1.38 g, 0.01 mol) for dye **1** or 4-aminophenol (1.09 g, 0.01 mol) for dye **2**, was prepared in concentrated HCl (3 mL). A cold aqueous solution of NaNO<sub>2</sub> (1.2 g) was added dropwise at 0–5 °C over 15 min, and the mixture was stirred for a further 30 min to generate the diazonium salt. This freshly prepared solution was then added slowly to a precooled ethanolic solution of pyrano[2,3-*c*]pyrazole intermediate **A** (3.44 g, 0.01 mol in 20 mL ethanol) over 1 h with vigorous stirring. Sodium acetate was added to facilitate dye precipitation. The resulting dyes were filtered, washed thoroughly with distilled water until acid-free, air-dried, and recrystallized from ethanol to afford dyes **1** and **2** in pure form.

#### 4.3.2.1. (*E*)-6-amino-4-(2-hydroxy-5-((3-nitrophenyl)diazenyl)phenyl)-3-methyl-1-phenyl-1,4-dihydropyrano[2,3-*c*]pyrazole-5-carbonitrile (**1**)

Chocolate brown powder; Yield: 76%; mp: 266-268 °C; IR (KBr)  $\text{cm}^{-1}$  $\nu_{\text{max}}$ : 3420 (OH), 3320, 3240 (NH<sub>2</sub>), 3054, 2925, 2205 (CN), 1650 (C=N), 1605, 1580 (C=C), 1515 (N=N), 1525, 1345, 1525 (NO<sub>2</sub> asym./sym.); <sup>1</sup>H NMR (500 MHz, DMSO-*d*<sub>6</sub>)  $\delta$  (ppm): 9.35 (br.s, 1H, OH), 7.55–8.94 (m, 12H, Ar-H), 6.96 (s, 2H, NH<sub>2</sub>), 4.82 (s, 1H, C<sub>4</sub>-H, pyran), 2.02 (s, 3H, CH<sub>3</sub>); <sup>13</sup>C NMR (125 MHz, DMSO-*d*<sub>6</sub>)  $\delta$  (ppm): 165.9 (C<sub>6</sub>-NH<sub>2</sub>), 160.8, 158.9, 158.8, 157.4, 153.5, 152.8, 144.2, 141.8, 136.9, 134.5, 133.1, 130.4 (2C), 129.6, 122.3 (2C), 120 (CN), 119.9, 119.86, 117.3, 112.7, 108.3, 59 (C<sub>5</sub>-CN), 23.1 (C<sub>4</sub>, pyran), 12.1 (CH<sub>3</sub>); EIMS, *m/z* [M]<sup>+</sup> calcd: 493.15; found: 493.19; Elemental Analysis for C<sub>26</sub>H<sub>19</sub>N<sub>7</sub>O<sub>4</sub> (%), Calcd: C, 63.28; H, 3.88; N, 19.87; found: C, 63.24; H, 3.89; N, 19.82.

#### 4.3.2.2. (*E*)-6-amino-4-(2-hydroxy-5-((4-hydroxyphenyl)diazenyl)phenyl)-3-methyl-1-phenyl-1,4-dihydropyrano[2,3-*c*]pyrazole-5-carbonitrile (**2**)

Brownish red powder; Yield: 78%; mp: 278-280 °C; IR (KBr)  $\text{cm}^{-1}$  $\nu_{\text{max}}$ : 3405 (OH), 3310 (NH<sub>2</sub> asym.), 3228 (OH), 3047, 2922, 2206 (CN), 1650 (C=N), 1601, 1586 (C=C), 1514 (N=N), 1278, 1152 (C–O, phenolic); <sup>1</sup>H NMR (500 MHz, DMSO-*d*<sub>6</sub>)  $\delta$  (ppm): 9.85 (br.s, 1H, OH, phenolic group adjacent to azo linkage), 9.2 (br.s, 1H, OH, terminal para-phenolic group), 7.4-8.79 (m, 12H, Ar-H), 6.81 (s, 2H, NH<sub>2</sub>), 4.68 (s, 1H, C<sub>4</sub>-H, pyran), 1.94 (s, 3H, CH<sub>3</sub>); <sup>13</sup>C NMR (125 MHz, DMSO-*d*<sub>6</sub>)  $\delta$  (ppm): 163.83 (C<sub>6</sub>-NH<sub>2</sub>), 158.59, 156.73, 156.52, 155.35, 150.79, 142.24, 139.84, 134.94, 132.53, 131.63, 128.35 (2C), 127.53 (2C), 120.24 (2C), 118.1 (CN), 117.83, 117.81, 115.25 (2C), 110.63, 58.82 (C<sub>5</sub>-CN), 22.9 (C<sub>4</sub>, pyran), 12.31 (CH<sub>3</sub>); EIMS, *m/z* [M]<sup>+</sup> calcd: 464.16; found: 464.2; Elemental Analysis for C<sub>26</sub>H<sub>20</sub>N<sub>6</sub>O<sub>3</sub> (%), Calcd: 67.23; H, 4.34; N, 18.09; found: C, 67.18; H, 4.29; N, 18.04.

#### 4.3.3 Synthesis of (*E*)-6-amino-4-(4-methoxy-3-((4-nitrophenyl)diazenyl)phenyl)-3-methyl-1-phenyl-1,4-dihydropyrano[2,3-*c*]pyrazole-5-carbonitrile (**3**)

To 4-nitroaniline (1.38 gm, 0.01 mol) ice cold solution in conc. HCl (3 mL), a cold aq. soln. of NaNO<sub>2</sub> (1.2 gm), was supplemented at 0-5 °C and dropwise within 15 min and stirred for further 30 min yielding the diazonium salt solution which then supplemented to pre-cooled solution of pyrano[2,3-*c*]pyrazole congener (3.58 gm, 0.01 mol, in 20 mL ethanol) (**B**) dropwise over a period of 1 h with enthusiastic stirring and inserting CH<sub>3</sub>COONa for piling up the dye particles. The formed dye was filtered, washed with water till it was acid-free, and dry up at room temperature and recrystallized from ethanol to yield pyrano[2,3-*c*]pyrazole based Azo disperse dye (**3**).

Caramel powder; Yield: 78%; mp: > 300 °C; IR (KBr)  $\text{cm}^{-1}$  $\nu_{\text{max}}$ : 3380, 3305 (NH<sub>2</sub>), 3094, 2923, 2204 (CN), 1651 (C=N), 1603, 1582 (C=C), 1515 (N=N), 1528, 1344 (NO<sub>2</sub> asym./sym.), 1248 (C–O–CH<sub>3</sub>); <sup>1</sup>H NMR (500 MHz, DMSO-*d*<sub>6</sub>)  $\delta$  (ppm): 7.4-8.8 (m, 12H, Ar-H), 6.81 (s, 2H, NH<sub>2</sub>), 4.74 (s, 1H, C<sub>4</sub>H, pyran), 3.83 (s, 3H, OCH<sub>3</sub>), 1.93 (s, 3H, CH<sub>3</sub>); <sup>13</sup>C NMR (125

MHz, DMSO- $d_6$ )  $\delta$  (ppm): 164.55 (C<sub>6</sub>-NH<sub>2</sub>), 159.3, 157.44, 157.23, 156.06, 151.5, 142.95, 140.55, 135.65 (2C), 133.24, 132.34 (2C), 129.06 (2C), 128.24 (2C), 120.95 (CN), 118.78, 118.54, 118.52, 115.96, 111.34, 61.63 (C<sub>5</sub>-CN), 59.55 (OCH<sub>3</sub>), 23.63 (C<sub>4</sub>, pyran), 13.03 (CH<sub>3</sub>); EIMS,  $m/z$  [M]<sup>+</sup> calcd: 507.17; found: 507.18; Elemental Analysis for C<sub>27</sub>H<sub>21</sub>N<sub>7</sub>O<sub>4</sub> (%), Calcd: C, 63.90; H, 4.17; N, 19.32; found: C, 63.86; H, 4.2; N, 19.36.

#### 4.4. Dyeing Procedures

Polyester and nylon fabrics were dyed using a high-temperature high-pressure method, whereas wool fabrics were dyed in a conventional water bath at a liquor ratio of 50:1. Dyes **1–3** were applied at a 2% shade. Each dye was dissolved in 1 mL DMF prior to addition to the dye bath under continuous stirring to ensure homogeneous dispersion.

After dyeing, the samples were washed in a solution containing 5 g L<sup>-1</sup> non-ionic detergent at 50 °C for 30 min, rinsed thoroughly with distilled water, and air-dried at ambient temperature.<sup>28–38</sup>

#### 4.5. Colour Measurements

Colour strength and coordinates were measured using a CE-7000A reflectance spectrophotometer with BaSO<sub>4</sub> as standard and a D65/10° illuminant–observer combination. K/S values and CIE Lab parameters were calculated from the reflectance data, and each value represents the mean of three measurements.

K/S values were calculated according to the Kubelka–Munk (**Eq. 1**):

$$K/S = (1-R)^2 / 2R \quad (1)$$

where **K** is the absorption coefficient, **S** is the scattering coefficient, and **R** is the reflectance at  $\lambda_{max}$ .

#### 4.6. Scanning Electron Microscope (SEM)

SEM images were recorded using a Quanta FEG-250 system operated at 10–20 kV and analyzed using JEOL JSM-5310 and VEGA-3 TESCAN instruments.

#### 4.7. UV Protection Factor

UPF values were determined according to AS/NZS 4366:1996 and classified as Good (15–24), Very Good (25–39), or Excellent (> 40).

#### 4.8. Fastness Testing

The colored samples were first washed with 2 g L<sup>-1</sup> non-ionic detergent at 80 °C for 30 min. Subsequently, wash, light, rubbing, and perspiration fastness were evaluated according to ISO standard methods. Wash fastness was assessed using ISO 105-C02 (1989). Rubbing fastness (crocking) was evaluated using ISO 105-X12 (1987). Perspiration fastness was determined following ISO 105-E04 (1989) under both acidic and alkaline conditions. For each test, colour change was rated using AATCC Evaluation Procedure (EP) 1 (comparable to ISO 105-A02), while colour staining was rated using AATCC EP 2 (comparable to ISO 105-A03). Light fastness was assessed according to ISO 105-B02 (carbon arc).

#### 4.9. Determination of the Antimicrobial Activity

The antimicrobial activity of the tested compounds was evaluated using the agar diffusion assay by measuring the inhibition zone diameters (mm) against selected bacterial and fungal strains.<sup>39,40</sup>

The antimicrobial activity was investigated by the well agar diffusion method. Briefly, 2 mg of each compound was dissolved in 1 mL DMSO. The test microorganisms included *Staphylococcus aureus* ATCC 6538-P (Gram-positive) and *Escherichia coli* ATCC 25933 (Gram-negative), as well as *Candida albicans* ATCC 10231 (yeast) and *Aspergillus niger* NRRL-A326 (fungus). Nutrient agar plates were uniformly inoculated with 0.1 mL of microbial suspension (10<sup>5</sup>–10<sup>6</sup> cells mL<sup>-1</sup>) for bacteria and yeast. For antifungal evaluation, potato dextrose agar plates were seeded with 0.1 mL of fungal inoculum (10<sup>6</sup> cells mL<sup>-1</sup>). Wells of 0.5 cm diameter were made in the solidified agar, and 100  $\mu$ L of each prepared sample solution was introduced into each well. Plates were kept at 4 °C for 2–4 h to allow diffusion, then incubated at 37 °C for 24 h for bacteria and at 30 °C for 48 h for fungi and yeast. Antimicrobial activity was determined by measuring the diameter of the clear inhibition zone in millimeters. All experiments were performed more than once, and the mean values were recorded.

## References

- 1 Anik H. R., Tushar S. I., Mahmud S., Khadem A. H., Sen P., and Akter M. (2025) Into the revolution of nanofusion: merging high performance and aesthetics by nanomaterials in textile finishes. *Adv. Mater. Interfaces.*, 12 (1) 2400368.
- 2 Ding Y., Jiang J., Wu Y., Zhang Y., Zhou J., Zhang Y., and Zheng Z. (2024) Porous conductive textiles for wearable electronics. *Chem. Rev.*, 124 (4) 1535–1648.
- 3 El-Assaly S., Ismail A. E. H. A., Bary H., and Abouelenein M. (2021) Synthesis, molecular docking studies, and antimicrobial evaluation of pyrano[2,3-*c*]pyrazole derivatives. *Curr. Chem. Lett.*, 10 (3) 309–328.
- 4 Abouelenein M. G., Ismail A. E. H. A., Aboelnaga A., Tantawy M. A., El-Ebiary N. M., and El-Assaly S. A. (2023) Synthesis, DFT calculations, in silico studies, and biological evaluation of pyrano[2,3-*c*]pyrazole and pyrazolo[4',3':5,6]pyrano[2,3-*d*]pyrimidine derivatives. *J. Mol. Struct.*, 1275 134587.
- 5 Abdel-Megid M., Ali, T. E., Salem, M. E., Abouelenein, M. G., Nassar, I. F., Zaki, M. E. (2025) Ring-Chain Tautomerism (Part II): Synthetic Applications of Biologically Active Five-Membered Heterocycles with Two Heteroatoms. *J. Heterocycl. Chem.*, 62(12) 1939-1957.
- 6 Upadhyaya K., Shruti Sharma R., Dwivedi J. (2026) Recent Advances in the Synthesis of Biologically and Pharmaceutically Active Thiazole and Its Analogues. *J. Heterocycl. Chem.*
- 7 Allayeh A. K., El-Boghdady A. H., Said M. A., Saleh M. G., Abdel-Aal M. T., and Abouelenein M. G. (2024) Discovery of pyrano[2,3-*c*]pyrazole derivatives as novel potential human coronavirus inhibitors: design, synthesis, in silico, in vitro, and ADME studies. *Pharmaceuticals*, 17 (2) 198.
- 8 Abouelenein M. G., El-Boghdady A. H., Ali H. M., and Said M. A. (2024) Molecular investigations of novel pyrano[2,3-*c*]pyrazole congeners as potential HCoV-229E inhibitors: synthesis, molecular modeling, 3D QSAR, and ADMET screening. *Polycycl. Aromat. Compd.*, 1–18.
- 9 Abdel-Megid M., Salem M. E., El-Boghdady A. H., El-Rashedy A. A., Abdel-Aal M. T., Nassrallah A., and Abouelenein M. G. (2025) Novel pyrano[2,3-*c*]pyrazole derivatives: synthesis, spectroscopic characterization, and *in silico* evaluation of interactions with VEGFR-1 and aromatase. *J. Mol. Struct.*, 143107.
- 10 Ragheb A., Helal M., Abd El-magied S. A. E. R., Mohamed F. A. (2026). Bisazo Pyrano [2, 3-*c*] pyrazole Dyes: Structural Insights, Dyeing Performance, and Nanofinish-Enhanced Antibacterial Functionality in Textiles. *Egypt. J. Chem.*
- 11 Abouelenein M. G., Abdeen M. M., El-Shamy O. A., Mohsen Q., and Deyab M. A. (2025) Pyranopyrazole derivative, a new corrosion inhibitor designed for managing the corrosion problem of aluminum metal in alkaline solution. *Electrochim. Acta*, 514 145675.
- 12 Kanwal F., Javed T., Hussain F., Wasim M., and Batool M. (2024) Enhanced dye photodegradation through ZnO and ZnO-based photocatalysts doped with selective transition metals: a review. *Environ. Technol. Rev.*, 13 (1) 754–793.
- 13 Nawaz A., Farhan A., Maqbool F., Ahmad H., Qayyum W., Ghazy E., and Fathi-Karkan S. (2024) Zinc oxide nanoparticles: pathways to micropollutant adsorption, dye removal, and antibacterial actions- A study of mechanisms, challenges, and future prospects. *J. Mol. Struct.*, 138545.
- 14 Ramesh N., Lai C. W., Johan M. R. B., Mousavi S. M., Badruddin I. A., Kumar A., and Gapsari F. (2024) Progress in photocatalytic degradation of industrial organic dye by utilising the silver-doped titanium dioxide nanocomposite. *Heliyon*, 10 (24).
- 15 Gharanjig K., Gharanjig H., Imani H., and Goudarzi S. (2024) Nanopigments in textiles. In *Nanotechnology in Textile Finishing: Advancements and Applications*, pp. 123–163, Springer Nature Singapore, Singapore.
- 16 Ibrahim H. M., El-magied A., Abd El-Raouf S., Mohamed F. A., Aboelenien M. G. (2025) Advanced Pyrano [2, 3-*c*] Pyrazole-based azo dyes: enhanced dyeing performance and antibacterial activity of wool, polyester and nylon fabrics via gold nanoparticle functionalization. *Egypt. J. Chem.*, 69 (1) 261-278.
- 17 Mohamed F. A., El-Megied S. A. A., Abouelenein M. G., El-Sawy E. R. (2026) New Azo Disperse Dyes Based on 1H-Phenanthro [9, 10-*d*] imidazole: Synthesis, Antibacterial Activity, ADME Study, and Molecular Docking. *Fiber. Polym.*, 1-17.
- 18 Nassar I. F., Abdel-Rahman A. A. H., Elnemr E. M., Said M. A., and Abouelenein M. G. (2024) Facile synthesis, in silico studies, and biological assessment of novel pyrazolo[3,4-*b*]pyridine congeners. *Egypt. J. Chem.*, 67 (11) 83–97.
- 19 Abouelenein M. G., El-Rashedy A. A., Awad H. M., El-Farargy A. F., Nassar I. F., and Nassrallah A. (2023) Synthesis, molecular modeling insights, and anticancer assessment of novel polyfunctionalized pyridine congeners. *Bioorg. Chem.*, 141 106910.
- 20 Abouelenein M. G., Mohamed M. B. I., Elsenety M. M., El-Rashedy A. A., Ghalib S. H., Mohamed F. A. E., and Ageeli A. A. (2024) Facile and novel synthetic approach, molecular docking, molecular dynamics, and drug-likeness evaluation of 9-substituted acridine derivatives as dual anticancer and antimicrobial agents. *Chem. Biodivers.*, 21 (5) e202301986.
- 21 Rabiei K. (2025) Recent application of clay-based heterogeneous catalyst in organic reactions. *J. Inorg. Organomet. Polym. Mater.*, 35 (1) 1-22.

- 22 Ibrahim H. M., El-Magied A., Abd El-Raouf S., Mohamed F. A., and Aboelenien M. G. (2025) Advanced pyrano[2,3-*c*]pyrazole-based azo dyes: enhanced dyeing performance and antibacterial activity of wool, polyester and nylon fabrics *via* gold nanoparticle functionalization. *Egypt. J. Chem.*, 69 (1) 261-278.
- 23 Khayer K. Haque, T. (2020) Density Functional Theory Calculation on the Structural, Electronic, and Optical Properties of Fluorene-Based Azo Compounds. *ACS Omega*, 5(10), 4507-4531.
- 24 Emanuele L., D'Auria M. (2024) The use of heterocyclic azo dyes on different textile materials: a review. *Organics*, 5(3), 277-289.
- 25 Yordanov D., Nakashima K., Smolka R., Matsushima Y., Hirashima S. I., Vala M., Georgiev A. (2025) Visible Light Switching of Ortho-Functionalized Azo Phthalimides with Tunable Z-Isomer Stability. *J. Org. Chem.*, 90(37), 12904-12915.
- 26 Lv S., Zhang Y., Zhang S., Tang B. (2026) Visible-Light-Driven Heteroaryl Azo Switches with High-Efficiency Photoisomerization for Advanced Photochromic Systems. *Adv. Opt. Mater.*, e03223.
- 27 Ibrahim H. M., Zaghoul S., Hashem M., and El-Shafei A. (2021) A green approach to improve the antibacterial properties of cellulose based fabrics using *Moringa oleifera* extract in presence of silver nanoparticles. *Cellulose*, 28 (1) 549-564.
- 28 Mohamed F. A., El-Megied S. A., Ibrahim H. M., and Shaban E. (2022) Synthesis, application, and antibacterial activity of new direct dyes based on chromene derivatives. *Curr. Org. Synth.*, 19 (6) 757-766.
- 29 Mohamed F. A., Abd El-Megied S. A., Bashandy M. S., and Ibrahim H. M. (2018) Synthesis, application and antibacterial activity of new reactive dyes based on thiazole moiety. *Pigment Resin Technol.*, 47 (3) 246-254.
- 30 Mohamed F. A., Shaban E., and Ibrahim H. M. (2022) Synthesis and antibacterial activity of some novel nucleus N-aminorhodanine based bis monofunctional and bifunctional reactive dyes and their application on wool and cotton fabrics. *Egypt. J. Chem.*, 65 (2) 597-608.
- 31 Mohamed F. A., Reda M. M., and Ibrahim H. M. (2022) Enhancement of Dyeing and Antimicrobial Properties of Chitosan and Chitosan Nanoparticles-Treated Cotton and Viscose Fabrics with Acid Dyes. *Egypt. J. Chem.*, 65 (13) 339-344.
- 32 Mohamed F. A., Shaban E., Ismail A. A., and Attia O. A. (2022) Synthesis, Application and Antimicrobial Activity of New Acid Dyes Based on 3-Amino-2-thioxo-4-thiazolidinone Nucleus on Wool and Silk Fabrics. *Curr. Org. Synth.*, 19 (1) 166-176.
- 33 Mohamed F. A., Tawfik T. M., and Ibrahim H. M. (2023) Surface Modification of Cotton, viscose, and polyester/cotton blend fabrics using nano carboxyethylchitosan Before Dyeing with commercial acid dyes and Antimicrobial Activity Evaluation. *Egypt. J. Chem.*, 66 (13) 993-1000.
- 34 Al-Megrin W. A. I., El-khadragy M. F., Mohamed F. A., and Ibrahim H. M. (2023) Free Salt Dyeing by Treatment of Cotton Fabric Using Carboxyethyl Chitosan and Synthesized Direct Dyes to Enhance Dyeing Properties and Antibacterial Activity. *Curr. Org. Synth.*, 20 (8) 910-918.
- 35 Ibrahim S. A., Mohamed F. A., Ibrahim H. M., and Shaban E. (2024) Synthesis, Characterization, Antibacterial Activity, and Applications of Novel Reactive Disperse Rhodanine Dyes on Silk and Nylon Fabrics. *Fibers Polym.*, 25 (1) 243-255.
- 36 Mohamed F. A., El-Megied S. A., and Ali N. (2024) Dyeing of Polyester Fabrics with Eco-Friendly Modified Natural Dyes Using IR and Ultrasonic Methods without Mordants or Dispersion Agents. *Egypt. J. Chem.*, 67 (7) 389-395.
- 37 Al-Megrin W. A. I., Mohamed F. A., and Ahmed H. M. (2025) Effect of DBD Plasma/Zinc Oxide Nanoparticles on the Printability of Wool Fabric With Beetroot Peels as a Natural Dye. *Plasma Proc. Polym.*, 22 (2) 2400130.
- 38 Fathy H., Helal M. H., Abbas D., and Mohamed F. A. (2024) Synthesis and characterization of some new Schiff base azo disperse dyes based on chromene moiety for simultaneous dyeing and antimicrobial finishing. *Sci. Rep.*, 14 (1) 23164.
- 39 Ayesha M. N., Subramaniam S., and Islam S. S. (2025) Evaluation of the antibacterial and antifungal activities of the extracts of *Aerides multiflora* Roxb. a native medicinal orchid. *Biocatal. Agric. Biotechnol.*, 68 103706.
- 40 El Mouzazi I., Laghmari M., Iraqi O., Ghabbour I., Benali T., Hammani K., Bour A., and Khal-Layoun S. (2025) Phytochemical content, *in vitro* antioxidants and antimicrobial activities of *Daphne gnidium* L. leaves. *Sci. Afr.*, 30 e03000.



© 2026 by the authors; licensee Growing Science, Canada. This is an open access article distributed under the terms and conditions of the Creative Commons Attribution (CC-BY) license (<http://creativecommons.org/licenses/by/4.0/>).